Absorption of light through isolated and coupled resonances in horizontal InP nanowire arrays

LUND
UNIVERSITY

Ali Hosseinnia

Supervisor: Dr. Nicklas Anttu

Co-supervisor: Prof. Mats-Erik Pistol

Autumn 2014

For the rest of my life I will reflect on what light is.

- Albert Einstein

Table of Contents

Acknowledgements

I take immense pleasure in thanking my supervisor Dr. Nicklas Anttu for his patient, responsible, motivational and encouraging guidance throughout the project. I am grateful for his scientific inputs and continuous assistance. Further, I wish to express deep gratitude to Prof. Mats-Erik Pistol for letting me to be part of his research group and involving me in the highly stimulating and intellectual academic and research dialogues.

I am obliged to Prof. Dan Hessman, Coordinator of the Nano Science Specialization of the Physics Master Programme for his supportive advices throughout my master studies. I would also like to thank my peers at Department of Physics and Lund Tekniska Högskola for the inspiring scientific environment.

Above all, for their unceasing motivation and support, I am thankful to my wife Zara Saeidzadeh, my father Ghodratollah Hosseinnia and my mother Masoumeh Shaterian, without whom this thesis could not have been realized.

Abstract

We have studied the interaction of light with two types of closely related nanostructures: a single horizontal InP nanowire and an infinite periodic array of such nanowires. The study has been done theoretically by calculating the absorption cross section of the nanowires via a semi analytical method, the Mie theory, and two numerical methods, the scattering matrix method (SMM) and the finite element method (FEM) to perform electromagnetic modeling.

The absorption spectra obtained by the Mie theory show strong polarization dependency. Also, we have noticed that the peaks in the spectra red shift by increasing the radius of the nanowires. To study this redshift, we assumed that the nanowires can be seen as optical waveguides that can capture the light in certain eigenmodes much like a whispering gallery mode. Due to this, a semi analytical eigenfunction method has been employed to investigate the eigenmodes in the nanowire. The results show that the eigenmodes are the origin of the Mie resonances and redshift by increasing the radius of the nanowire.

By moving to study the optical response of the periodic array consisting of infinitely many nanowires, an additional set of optical resonances is introduced to the absorption in the nanowires. These resonances are due to Bragg grating condition for constructive interference of scattered light between neighboring nanowires, and these resonances depend on the period of the structure. These new resonances are called *lattice resonance* throughout this thesis.

We show that for specific combination of the period of the array and the radius of the constituent nanowires, the lattice resonances couple with the single nanowire resonances. This coupling can boost the absorption in the array by a factor of 18 compared to that in single nanowires. Through such resonant absorption, the nanowires can absorb 200 times stronger than the same amount of InP material in bulk form.

1. Introduction

In the 17th century, Francesco Maria Grimaldi performed experiments on the diffraction of light, which opened a new paradigm for optics [1]. His work was the beginning for breakthroughs in the wave-description of light, by passing the white light through apertures and claiming that light has fluidic properties and exhibits wavelike motion [2]. His work in extension laid the ground for research and development in all branches of optics, including light-matter interaction. An economically and commercially relevant application of light-matter interaction lies in the field of semiconductor photovoltaics and photodetectors. With the advent and rise of nanotechnology and nanomaterials, especially semiconductor nanowires, we can efficiently control the light-matter interaction; by designing the nanostructure geometry, we can tune and control the diffraction effects to enhance the interaction in a way not possible in bulk-like photovoltaic devices and photodetectors.

In the current work, we investigate the interaction of light with nanostructures, specifically semiconductor nanowires, and decipher the scattering and absorption mechanisms. Currently, a lot of research efforts have been spent on vertically aligned semiconductor nanowire arrays [3-6]. Consequently, a lot of research results exist for these structures. However, here we flip the system around and study horizontal nanowires. We find, via numerical and analytical methods, coupled optical resonances that can boost the absorption of light by a factor of 200.

1.1. Electromagnetic Optics

Depending on the physics of the problem, including the size of the object which is interacting with light and the specific scattering phenomena, Optics can be divided into three different theoretical areas: Ray Optics, Electromagnetic Optics, and Quantum Optics [7].

Ray Optics, which was the first to be introduced of these three descriptions, can explain the behavior of light that propagates in a matter system whose dimensions are much greater than the wavelength of the propagating light. The main principle of Ray Optics is that light rays travel between two points in the least or the maximum (e.g. when light travels from one focus of an elliptical mirror to another one by hitting the mirror at the minor axis in between, when the curvature of the mirror is slightly smaller than the ellipse at the point of impact [7]) amount of time. In this way, the optical path-length between two points, A and B, is defined by $\int_A^B n(\vec{r})\, dx$, with $n(\vec{r}) = \frac{C_0}{C(\vec{r})}$ the refractive index of the medium, $C(\vec{r})$ the speed of light in the medium, C_0 the speed of light in free space and dx the differential element of the path between A and B. Then the condition $\delta \int_A^B n(\vec{r})\, dx = 0$, with δ the variation of the path in the integral, defines the path the light will travel. Through this formalism, ray optics can explain, for example, the angles between the incident, refracted and the reflected light at an interface by the Snell's law [7]. The formalism of ray optics is therefore enough for explaining the working mechanism of refraction based optical elements, such as telescopes and microscopes.

However, ray optics fails to explain many optical phenomena, like the proportion of the reflected and the refracted light and many optics related to small objects with sizes comparable with the wavelength of the light. To explain these phenomena, we need the Electromagnetic or the Quantum Optics theory instead. The latter is beyond the scope of this research project and we neglect any possible quantum effects. Thus, we choose to exploit Electromagnetic Optics in this thesis.

Electromagnetic optics describes light as an electromagnetic wave that propagates in a medium. The wave consists of two perpendicular fields (electric $\vec{E}$ and magnetic $\vec{H}$ fields) normal to the propagation

direction (Fig. (1a)). These fields are coupled in the famous Maxwell's equations [8]. The source free Maxwell's equations, where the current density $\vec{J}$ and the free charge density ρ in a linear and homogenous medium are zero (and light is monochromatic, thus, the frequency ϑ of light is single valued and does not change during the scattering processes), are:

$$\vec{\nabla}\times \vec{E} = i\sqrt{\frac{\mu_0}{\varepsilon_0}}k\vec{H}, \tag{1}$$

$$\vec{\nabla}\times \vec{H} = -i\sqrt{\frac{\varepsilon_0}{\mu_0}}kn^2\vec{E}, \tag{2}$$

$$\vec{\nabla}\cdot \vec{E} = 0, \tag{3}$$

$$\vec{\nabla}\cdot \vec{H} = 0. \tag{4}$$

Here, $k = \frac{2\pi}{\lambda_0}$ is the angular wave number, λ_0 the wavelength of light in free space, ε_0 the vacuum permittivity, μ_0 the magnetic permeability and *n* the refractive index of the medium. Here, we also assume that the medium is nonmagnetic. The boundary conditions that are imposed at the transition region of two different mediums can be obtained from Eqs. (3), (4):

$$\left(\vec{E}_2(\vec{r}) - \vec{E}_1(\vec{r})\right)\times \hat{a} = 0, \tag{5}$$

$$\left(\vec{H}_2(\vec{r}) - \vec{H}_1(\vec{r})\right)\times \hat{a} = 0. \tag{6}$$

Here $\hat{a}$ is the normal unit vector of the boundary surface. Thus, Eqs. (5), (6) require that the tangential components of $\vec{E}$ and $\vec{H}$ are continuous across the boundary.

1.2. Plane waves

Throughout this work, we assume that all fields are time harmonic with frequency ω. In more detail, we assume that the incident light is a monochromatic homogenous electromagnetic plane wave which has the form of $\vec{E} = \vec{E}_0 e^{i\vec{K}\cdot\vec{r}-i\omega t}$ and $\vec{H} = \vec{H}_0 e^{i\vec{K}\cdot\vec{r}-i\omega t}$, where $\vec{K} = nk\hat{e}$ is the wave vector in the direction of the unit vector $\hat{e}$ parallel to the propagation direction, $\omega = 2\pi\vartheta$ is the angular frequency. $\vec{E}_0 = E_0\hat{e}_i$ and $\vec{H}_0 = H_0\hat{e}_j$ are the constant complex amplitudes of the wave in the direction of the unit vectors $\hat{e}_i$ and $\hat{e}_j$ where $\hat{e}_i \perp \hat{e}_j$, $\hat{e}_i \perp \hat{e}$, and $\hat{e}_j \perp \hat{e}$. The quantity $\vec{K}\cdot\vec{r} - \omega t$ is called the phase of the wave, and for a plane wave the phase increases linearly with frequency. Thus, a plane wave contains parallel constant surfaces given by $\vec{K}\cdot\vec{r} - \omega t = A$ (*A* a constant) that move with the phase velocity of $v = \frac{\omega}{nk}$, perpendicular to $\vec{K}$ [9].

If we substitute $\vec{E}$ and $\vec{H}$ for the plane wave into Eqs. (1)-(4) we derive the Maxwell equations for the plane waves:

$$\vec{K}\times \vec{E}_0 = i\sqrt{\frac{\mu_0}{\varepsilon_0}}k\vec{H}_0, \tag{7}$$

$$\vec{K}\times \vec{H}_0 = -i\sqrt{\frac{\varepsilon_0}{\mu_0}}kn^2\vec{E}_0, \tag{8}$$

$$\vec{K}\cdot \vec{E}_0 = 0, \tag{9}$$

$$\vec{K}\cdot \vec{H}_0 = 0. \tag{10}$$

Eqs. (7)-(10) emphasize the fact that $\vec{K}$, $\vec{H}_0$ and $\vec{E}_0$ are perpendicular to each other. From Eq. (5), we obtain a boundary condition specific for plane waves: The tangential component of $\vec{K}$ should be equal for both boundaries. This condition is illustrated in Fig. (1b) at the boundary of a cylindrical waveguide and its surrounding medium.

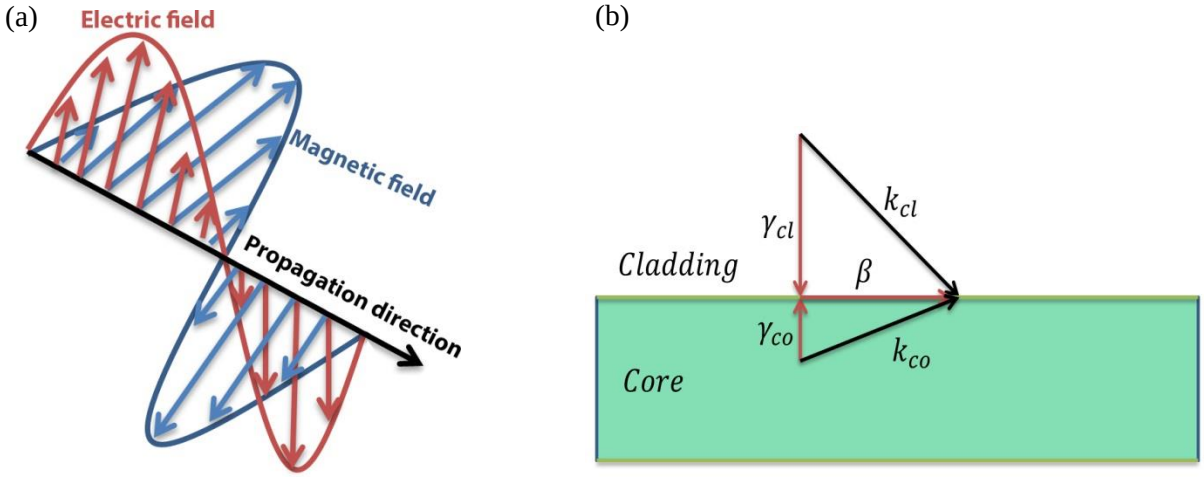

Figure 1. (a) An electromagnetic wave; the electric vector field (red arrows) and the magnetic vector fields (blue arrows) are perpendicular to each other and propagate in a direction perpendicular to both of them (black arrow). (b) A 2D schematic of a waveguide with different refractive indices for its core (green area) and cladding (white area). k_{cl} and k_{co} are the wave vectors in the core and the cladding respectively and γ_{cl} and γ_{co} are their normal components. β is the tangential component of the wave vectors, and it is equal in both the core and the cladding.

1.3. Incident, internal and scattered field

Fig. (2a) shows reflection, refraction and transmission by a slab, schematically. The refractive index of the surrounding medium and the slab are different. Inside the slab, the fields are reflected several times, and the new reflected fields can be refracted and transmitted themselves again. Considering the conservation of energy and the Snell's law, one can find a relation for the final intensities of light for the reflected, refracted and the transmitted fields by the help of the famous Fresnel law, which can be derived from the Maxwell equations [7].

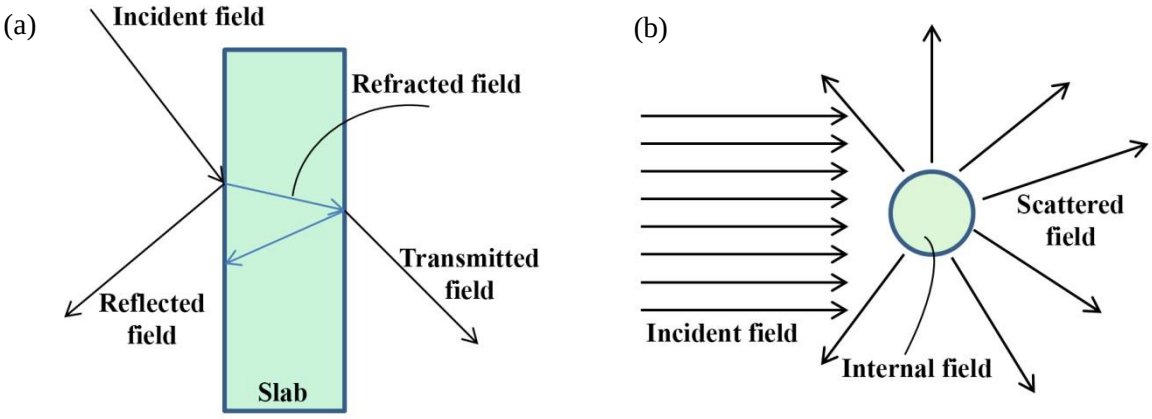

Figure 2. Schematics for (a) reflection, refraction and transition of light by a slab and (b) the scattering of light by a small particle which has a size comparable with the wavelength of the incoming light [9].

On the other hand, for a small particle, when the size of the object is comparable with the wavelength of the incident light, the fields are categorized in another way. The reflected and the transmitted fields

together now are called scattered fields and the refracted fields inside the particle are called internal fields [9]. This is illustrated schematically in Fig. (2b). To find information about these fields from the Maxwell's equations, several analytical and numerical calculations have been suggested for different systems. In this thesis, we use semi-analytical calculations; Mie Theory and Eigen Function Method, and numerical calculations; Finite Element Method (FEM) and Scattering Matrix Method (SMM) which are explained in more detail in Chapter 2. An example of such a modeling by FEM is presented in Fig. (3a) and (b). These results have been obtained with the Comsol Multiphysics software (see Section 2.3 for details) and show the norm of the electric field of a light that is scattered by an InAs nanowire with 1 μm length and 30 nm radius surrounded by air. Here we show the fields in the surrounding air medium (Fig. (2a)) and at the surface of the nanowire (Fig. (2b)).

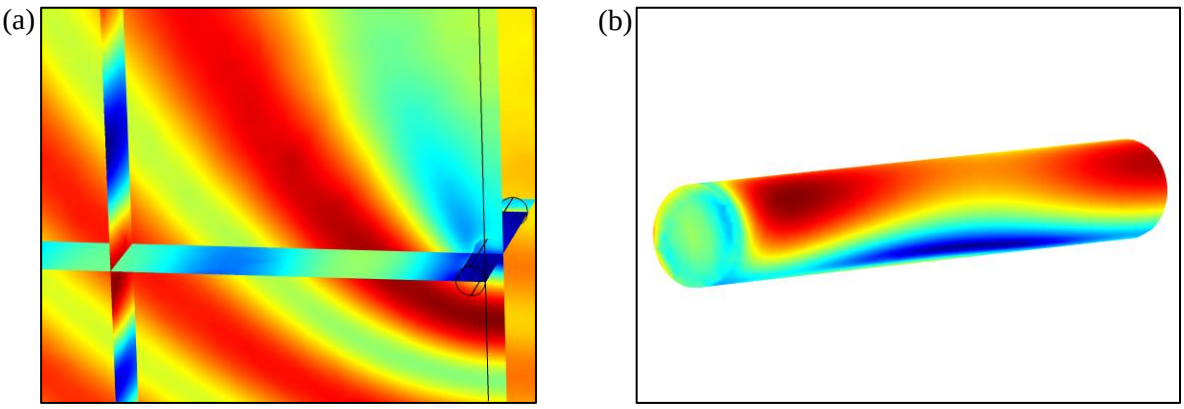

Figure 3. The norm of the scattered electric field by a 1 μm long InAs nanowire with 30 nm radius surrounded by air where the light incidents from the bottom. (a) Electric field in the medium at four different slices planes (the nanowire is lying at the middle right side of the plot and is transparent) and (b) at the surface of the same nanowire. The color bars and the scales are omitted for clarity.

1.4. Semiconductors

Semiconductors are solids with conductivity between insulators and conductors. This unique feature is possible via a property which is called the band gap E_g [10]. This property, that is different in each semiconductor, also makes them suitable candidate for opto-electronic devices such as photodetectors and photovoltaics. Semiconductors have two different energy bands for so called electron and holes, the valence and conduction band, respectively, which are separated by a forbidden energy gap or, in other words, the band gap. If an electron that lies in the valance band receives a photon with energy higher than the band gap energy, that is when $\hbar\omega \geq E_g$, the electron can absorb the photon and thus jump to the conduction band leaving a hole in the valence band. Then the electron in the conduction band can contribute to a current in an external circuit. On the other hand if the energy of the incident photon is less than E_g, the photon cannot be absorbed by electrons in the valence band and the semiconductor becomes transparent for the photon.

In general, there are two different types of energy band gaps in semiconductors; the direct and the indirect bandgap [11]. The characterization of the band energy states in conduction and valence band is done by studying how these energies vary with the momentum of the electrons and holes in the crystal (k-vector). Moreover, the transition of an electron from the valence band to the conduction band (or vice versa) fulfills the energy and the (crystal) momentum conservations at the same time. Photons carry a negligible amount of momentum, so the transitions occurred by them do not change the momentum of the electrons and directly change their energies. If the maximum energy state in the valence band has the same k-vector as the minimum energy state in the conduction band, a photon

with energy slightly above the band gap energy can transfer the electrons directly from the valence band to the conduction band. This signifies the direct band gap semiconductors like InAs and InP (Fig. (4a)).

On the other hand, in an indirect band gap semiconductor like Si and Ge, since the minimum energy state of the conduction band has a different k-vector than the maximum energy state of the valence band, a direct transition of electrons needs higher photon energy than the indirect band gap energy. But if another process that provides the change in the momentum, indirect transition from the maximum energy state in the valence band and the minimum energy state in the conduction band can happen. This additional process is performed by phonons, the vibrations of the crystal lattice in the semiconductor (Fig. (5b)).

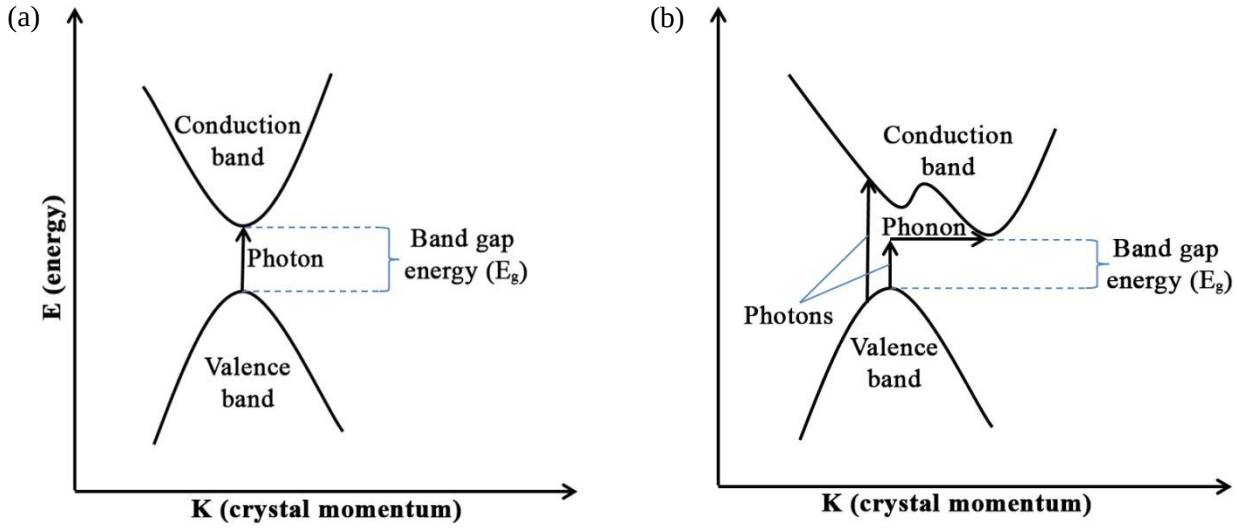

Figure 4. Transitions of electron via absorbing (a) a photon in a direct band gap and (b) a photon and a phonon in an indirect band gap semiconductor. Also a direct transition in an indirect band gap is illustrated in (b) which shows that it occurs when the photon energy is higher than the band gap energy [11].

There are several cost efficient opto-electronic devices like photovoltaic cells, photodetectors, light emitting diodes (LEDs) and lasers that take advantage of the inter-band transitions of electrons in semiconductors [7]. We briefly explain here the basics of a semiconductor photodetector and a photo voltaic cell as examples. A photodetector is a device that converts the photon energy to a measurable form like electric current that indicates the photon flux or the optical power. In a semiconductor photodetector, first the band gap energy should be less than the energy of a photon that is to be detected. When the electrons are moved into the conduction band and leave holes in the valence band, the excess electron-hole pairs are separated, by a built in electric field in the device which is enhanced by an external electric field that is applied over the device. Therefore, the electrons (and holes) can contribute to the current and this current can be measured by an ammeter.

In a photovoltaic cell, the basics are the same as in photodetectors but an external load (power converter) is needed to extract an output power from the generated current by the excess electron-hole pairs. Thus, in photovoltaics, the absorption of light gives rise to both a current and a voltage simultaneously.

1.5. Nanowires

Nanoscience offers a variety of options from nanoparticles to 2D thin films and 1D nanowires, for engineering and enhancing low cost and high efficient photo-devices with a lot less consumption of

the material [4, 12-15]. Although the lengths of the nanowires can vary a lot from a few ten nanometers to several micrometers depending on the application, their radii are mostly around 50-100 nm. In the study of light-matter interaction, specifically absorption applications, nanowire structures have shown significant advantages over conventional structures like thin films, by offering more absorption for a given amount of absorbing material and lower reflection losses [5, 6]. Another advantage of the nanowires is the high geometrical dependency of the absorption [16-18]. For example, in Section 2.4, we show how the optical resonances of a long nanowire depend on its radius and in the Appendix A we show how a variation in the length of the nanowire shifts these resonances. Therefore in summary, the advantages that attract scientists and engineers to study and explore the nanowires in different fields of physics are:

a) Geometry dependency of the optical properties of the nanowires which makes them tunable for the optical devices.
b) Large range of options in semiconductor materials with different band gap energies [19].
c) Very good control in the growth and fabrication of nanowire structures [20-23].

The latter, i.e. fabrication of nanowire structures, can be done in three different ways. First is to grow them individually and then transfer and deposit them on a substrate with pre-allocated places for the nanowires. The second way is to grow them directly with an ideal pattern on a substrate and the third way is to etch a bulk material to structure the nanowires in arbitrary design [24, 25].

Although a detailed description of the experimental methods of making nanowire structures is beyond the scope of this thesis, we mention the use of gold nanoparticles as catalysts in an epitaxial method called the vapor liquid solid (VLS) method. The nanowires are grown under these gold particles via chemical reactions of the growth precursors brought in as a gas vapor into the growth chamber. The positions of the gold particles can be engineered by different methods such as electron beam lithography (EBL), defining the position of the nanowires [25].

In Chapter 2 we describe two semi-analytical methods to investigate the normally incident light interaction with infinitely long horizontal single nanowires. We present there also two numerical methods to study the same interaction with an infinite periodic array of infinitely long nanowires. The choice of the normally incident light has been made with possible applications in mind. With normally incident light, the projected area of the opto-electronic device to the incident light is maximized. Although all the formula derivations and procedures in this work apply in general to any semiconductor material, we have chosen to use InP throughout. The band gap of InP (of energy $E_g = 1.34$ eV, corresponding to photons of wavelength λ_{bg} = 925 nm [19]) is very close to the visible wavelength range in the infrared region, which makes it interesting for a large class of photo-devices. In Chapter 3 we discuss the results for single nanowires and periodic array of infinitely long nanowires. There we show how the coupling of optical resonances in such a periodic nanostructures can boost the absorption by two orders of magnitude.

2. Methods and Theory

In this chapter we explain three different methods to find the absorption and scattering cross sections; the semi-analytical Mie Theory, and numerical calculations The Scattering Matrix Method (SMM) and The Finite Element Method (FEM). Also we explain the Eigenfunction Method as a semi-analytical way to find information about the fields and the eigenmodes.

2.1. The Mie Theory

Mie theory suggests solutions to the Maxwell's equations for light scattering by small particles [9, 26]. Here we thoroughly explain the principles of the light scattering by an infinitely long small cylinder. From Eqs. (1)-(4), if electric and magnetic fields fulfill the vector electromagnetic wave equations, they will also satisfy the Maxwell's equations. For a system like Fig. (1a), these vector wave equations for the fields in the core and the cladding are [8]:

$$\nabla^2\vec{E} + K^2\vec{E} = 0, \tag{11}$$
$$\nabla^2\vec{H} + K^2\vec{H} = 0. \tag{12}$$

We define two orthogonal vectors $\vec{M}$ and $\vec{N}$ that obey the source free Maxwell's equations like $\vec{E}$ and $\vec{H}$ above by requiring that:

$$\vec{\nabla} \times \vec{M} = nk\vec{N}, \tag{13}$$
$$\vec{\nabla} \times \vec{N} = nk\vec{M}, \tag{14}$$
$$\vec{\nabla} \cdot \vec{M} = \vec{\nabla} \cdot \vec{N} = 0. \tag{15}$$

To ascertain that $\vec{N}$ and $\vec{M}$ fulfill Eqs. (13)-(15), they should be the answers of $\nabla^2\vec{M} + n^2k^2\vec{M} = 0$ or $\nabla^2\vec{N} + n^2k^2\vec{N} = 0$ like the vector wave equations for the electric and magnetic fields from Maxwell equations. We introduce a scalar function f and a constant vector $\vec{a}$ where:

$$\vec{\mathrm{M}} = \vec{\nabla} \times (\vec{a}f). \tag{16}$$

The divergence of the curl of any vector is zero, so:

$$\vec{\nabla} \cdot \vec{M} = 0.$$

Considering $\vec{\nabla} \times \left(\vec{\nabla} \times \vec{M}\right) = \vec{\nabla}\left(\vec{\nabla} \cdot \vec{M}\right) - \vec{\nabla} \cdot \left(\vec{\nabla}\,\vec{M}\right)$ and $\nabla^2\vec{M} = \vec{\nabla} \cdot \left(\vec{\nabla}\,\vec{M}\right)$, we construct the vector wave equation for $\vec{M}$:

$$\nabla^2\vec{M} = -\,\vec{\nabla} \times \left(\vec{\nabla} \times \vec{M}\right) = -\,\vec{\nabla} \times \left(\vec{\nabla} \times \left(\vec{\nabla} \times (\vec{a}f)\right)\right).$$

By using $\vec{\mathrm{A}} \times \left(\vec{\mathrm{B}} \times \vec{C}\right) = \vec{\mathrm{B}}\left(\vec{\mathrm{A}} \cdot \vec{C}\right) - \vec{\mathrm{C}}\left(\vec{\mathrm{A}} \cdot \vec{B}\right)$ and $\vec{\nabla} \cdot \left(\varphi\vec{A}\right) = \varphi\,\vec{\nabla} \cdot \vec{A} + \vec{A}\,\vec{\nabla}\,\varphi$, we can write:

$$\nabla^2\vec{M} = -\,\vec{\nabla} \times \vec{\nabla}\left(\vec{a} \cdot \vec{\nabla}f\right) + \vec{\nabla} \times (\vec{a}\nabla^2 f).$$

The curl of a gradient is zero for any vector. Thus, $\vec{\nabla} \times \vec{\nabla}\left(\vec{a} \cdot \vec{\nabla}f\right)$ vanishes in the above equation and we write:

$$\nabla^2\vec{M} + n^2k^2\vec{M} = \vec{\nabla} \times \left(\vec{\mathrm{a}}\,(\nabla^2 f + n^2k^2 f)\right). \tag{17}$$

From Eq. (17), if f satisfies the scalar wave equation $\nabla^2 f + n^2 k^2 f = 0$, then $\vec{M}$ is an answer to the vector wave equation. Usually f is called the generating function while $\vec{a}$ is called the guiding vector.

Therefore, we aim to solve:

$$\nabla^2 f + n^2 k^2 f = 0, \tag{18}$$

in cylindrical coordinate. Expanding ∇^2 in the cylindrical components yields:

$$\frac{\partial^2 f}{\partial r^2} + \frac{1}{r}\frac{\partial f}{\partial r} + \frac{1}{r^2}\frac{\partial^2 f}{\partial \varphi^2} + \frac{\partial^2 f}{\partial z^2} + k^2 n^2 f = 0. \tag{19}$$

The symmetry of the system (that is, the cylindrical symmetry of $n(r, \theta, z) = n(r)$) allows us to separate the variables in the form of $f = R(r)\emptyset(\varphi)Z(z)$. This gives:

$$\frac{1}{Z}\frac{d^2 Z}{dz^2} = -\left(\frac{1}{R}\frac{d^2 R}{dr^2} + \frac{1}{r}\frac{1}{R}\frac{dR}{dr} + \frac{1}{r^2}\frac{1}{\varphi}\frac{d^2\emptyset}{d\varphi^2} + k^2 n^2\right). \tag{20}$$

Since r and θ are arbitrary, $\frac{1}{Z}\frac{d^2 Z}{dz^2} = \beta^2$ with β a constant must hold, with the answer of the form $\exp(i\beta z)$. Notice that we consider normal illumination, in which case the *K* vector of the incident light is perpendicular to $\hat{z}$ (the direction of the axis of the cylinder). Therefore, β_{inc}, the propagation constant of the incident light along the cylinder axis is zero. From the boundary condition of the Maxwell's equations for plane waves (see Section 1.2), $\beta = \beta_{\text{inc}} = 0$ both inside as well as outside of the cylinder and $e^{i\beta z} = 1$. By substituting the LHS of Eq. (20) with zero we have:

$$\frac{1}{\varphi}\frac{d^2\emptyset}{d\varphi^2} = \frac{r^2}{R}\frac{d^2 R}{dr^2} + \frac{r}{R}\frac{dR}{dr} + r^2 k^2 n^2. \tag{21}$$

By setting the LHS of Eq. (21) to $\frac{1}{\varphi}\frac{d^2\emptyset}{d\varphi^2} = -\vartheta^2$, we find the solution in the form of $\emptyset(\varphi) = \exp(i\vartheta\varphi)$ for the φ dependent part of f . Moreover, from the symmetry, since $\emptyset(\varphi + 2\pi) = \emptyset(\varphi)$, ϑ should be an integer, and then we are left with:

$$\frac{d^2 R}{dr^2} + \frac{1}{r}\frac{dR}{dr} + \left(k^2 n^2 - \frac{\vartheta^2}{r^2}\right)R = 0. \tag{22}$$

The general solution for Eq. (22) is in the form of $L_\vartheta(knr)$ that is a Bessel or Hankel function of the first or the second kind [27] and from that the general answer for Eq. (19) can be written as:

$$f(r, \varphi, z) = L_\vartheta(knr)e^{i\vartheta\varphi} \qquad (\vartheta = 0, \pm 1, \pm 2, \dots). \tag{23}$$

Now from the symmetry of the cylinder, if we choose $\vec{a} = \hat{z}$, and use the definition of the curl operator in the cylindrical coordinate which is:

$$\vec{\nabla} \times \vec{A} = \left(\frac{1}{r}\frac{\partial \vec{A}_z}{\partial \varphi} - \frac{\partial \vec{A}_\varphi}{\partial z}\right)\hat{r} + \left(\frac{\partial \vec{A}_r}{\partial z} - \frac{\partial \vec{A}_z}{\partial r}\right)\hat{\varphi} + \frac{1}{r}\left(\frac{\partial (r\vec{A}_\varphi)}{\partial r} - \frac{\partial \vec{A}_r}{\partial \varphi}\right)\hat{z},$$

the vector cylindrical harmonics $\vec{M}_\vartheta$ can be derived immediately from Eq. (16) and Eq. (23):

$$\vec{M}_\vartheta = e^{i\vartheta\varphi}\left[\frac{i\vartheta}{r}L_\vartheta(knr)\hat{r} - knL'_\vartheta(knr)\hat{\varphi}\right], \tag{24}$$

where the prime sign denotes the derivative with respect to the argument (knr). To find $\vec{N}_\vartheta$ we use Eq. (13):

$$\vec{N}_\vartheta = -e^{i\vartheta\varphi}\left[knL''_\vartheta(knr) + \frac{1}{r}L'_\vartheta(knr) - \frac{\vartheta^2}{knr^2}L_\vartheta(knr)\right]\hat{z}. \tag{25}$$

If we substitute *R* in Eq. (22) by $L_\vartheta(knr)$, we will end up with:

$$knL''_\vartheta(knr) + \frac{1}{r}L'_\vartheta(knr) - \frac{\vartheta^2}{knr^2}L_\vartheta(knr) + knL_\vartheta(knr) = 0.$$

Rewriting Eq. (24) after adding and subtracting $L_\vartheta(knr)$ inside the bracket and using the above equation gives:

$$\vec{N}_\vartheta = e^{i\vartheta\varphi}knL_\vartheta(knr)\hat{z}. \tag{26}$$

Now that we derived an expression for the vector harmonics, we expand the incident, internal and the scattered field on the bases of $\vec{M}_\vartheta$ and $\vec{N}_\vartheta$. The first step is to expand the incident electric field:

$$\vec{E}_i = \sum_{\vartheta=-\infty}^{\infty}\left[A_\vartheta\vec{M}_\vartheta + B_\vartheta\vec{N}_\vartheta\right], \tag{27}$$

Since the incident electric field covers all the space including $r = 0$, and the Bessel functions of the second kind, $\vec{Y}_\vartheta$, diverge at this point, the harmonics should be generated by f in the form of the Bessel functions of the first kind $\vec{J}_{\vartheta(knr)}$. Here, we consider the two main linear polarizations for normally incident light: one is the transverse electric (TE), where the electric field of the incoming wave has only the components which are transverse to the axis of the cylinder; and the other is transverse magnetic (TM) where the electric field has only the longitudinal component and the magnetic field contains only the transvers components

For TM polarization we write:

$$\vec{E}_{i\_TM} = \sum_{\vartheta=-\infty}^{\infty}\left[A_\vartheta\vec{M}_\vartheta + B_\vartheta\vec{N}_\vartheta\right]. \tag{28}$$

From the definition of the TM polarization and Eq. (24), $\vec{E}_{i\_TM}$ is perpendicular to $\vec{M}_\vartheta$, thus, $A_\vartheta = 0$. To find B_ϑ we use the orthonormality condition of the function $\emptyset(\varphi) = e^{i\vartheta\varphi}$ inside the harmonics, thus:

$$\int_0^{2\pi}\vec{E}_{i\_TM}\cdot\hat{z}e^{-i\vartheta\varphi}\,d\varphi = \int_0^{2\pi}\sum_{\alpha=-\infty}^{\infty}\left[B_\vartheta\vec{N}_\vartheta\cdot\hat{z}e^{-i\vartheta\varphi}\right]d\varphi \tag{29}$$

where $\vec{N}_\vartheta = e^{i\alpha\varphi}knJ_\vartheta(knr)\hat{z}$. The RHS of Eq. (29) is zero for all terms except for $\alpha = \vartheta$. Also from the assumption that $\vec{E}_{i\_TM}$ is a plane wave, it can be written as $\vec{E}_{i\_TM} = E_0e^{-(in_{cl}krcos\varphi)}\hat{z}$, where n_{cl} is the refractive index of the cladding or the surrounding medium . The *K* vector is normal to $\hat{z}$ and it is in $-\hat{e}_x$ direction (Fig. (5)). From these, Eq. (29) can be rewritten, so that:

$$\int_0^{2\pi}E_0e^{-i(n_{cl}krcos\varphi+\vartheta\varphi)}\,d\varphi = 2\pi B_\vartheta kn_{cl}\,J_\vartheta(kn_{cl}r).$$

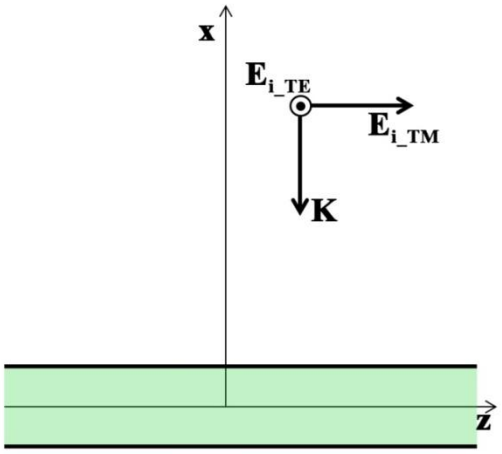

Figure 5. Schematic for the incident electric fields of the TE and TM polarized light ($\mathbf{E_{i\_TE}}$ and $\mathbf{E_{i\_TM}}$ respectively) and the $\boldsymbol{K}$ vector. The cylinder with refractive index of n_{co} is elongated in the z direction (green area).

From the integral form of the Bessel functions [28], the LHS is equal to $2\pi(-i)^{\vartheta}J_{\vartheta}(kn_{cl}r)$ and from that we can find an expression for B_{ϑ}:

$$B_{\vartheta} = \frac{E_0(-i)^{\vartheta}}{n_{cl}k}. \tag{30}$$

Thus, the electric field is:

$$\vec{E}_{i\_TM} = E_0 \sum_{\vartheta=-\infty}^{\infty}\left[(-i)^{\vartheta}e^{i\vartheta\varphi}J_{\vartheta}(kn_{cl}r)\right]\hat{z}. \tag{31}$$

From the Maxwell's equations (Eqs. (1)-(4)), $\vec{H}_{i\_TM} = ik\sqrt{\frac{\varepsilon_0}{\mu_0}}\,\vec{\nabla}\times\vec{E}_{i\_TM}$. After deriving the curl, the incident magnetic field for the TM polarization is:

$$\vec{H}_{i\_TM} = -iB_{\vartheta}\sqrt{\frac{\varepsilon_0}{\mu_0}}\sum_{\vartheta=-\infty}^{\infty}\left[\left(\frac{i\vartheta n_{cl}}{r}J_{\vartheta}(kn_{cl}r)\hat{r} - {n_{cl}}^2 kJ'_{\vartheta}(kn_{cl}r)\hat{\varphi}\right)e^{i\vartheta\varphi}\right],$$

which by substituting B_{ϑ} from Eq. (30) can be rewritten as:

$$\vec{H}_{i\_TM} = \sqrt{\frac{\varepsilon_0}{\mu_0}}E_0\sum_{\vartheta=-\infty}^{\infty}\left[(-i)^{\vartheta+1}\left(\frac{i\vartheta n_{cl}}{kr}J_{\vartheta}(kn_{cl}r)\hat{r} - n_{cl}J'_{\vartheta}(kn_{cl}r)\hat{\varphi}\right)e^{i\vartheta\varphi}\right]. \tag{32}$$

For the TE polarization, since the incident electric field $\vec{E}_{i\_TE}$ is perpendicular to $\vec{N}_{\vartheta}$, then from Eq. (27) $B_{\vartheta} = 0$. Using the same analogy of the TM polarization yields an expression for A_{ϑ}:

$$A_{\vartheta} = \frac{(-i)^{\vartheta+1}}{kn_{cl}}E_0, \tag{33}$$

and the fields for the TE polarizations are:

$$\vec{E}_{i\_TE} = E_0\sum_{\vartheta=-\infty}^{\infty}\left[(-i)^{\vartheta+1}\left(\frac{i\vartheta}{n_{cl}kr}J_{\vartheta}(kn_{cl}r)\hat{r} - J'_{\vartheta}(kn_{cl}r)\hat{\varphi}\right)e^{i\vartheta\varphi}\right], \tag{34}$$

$$\vec{H}_{i\_TE} = -E_0 n_{cl}\sqrt{\frac{\varepsilon_0}{\mu_0}}\sum_{\vartheta=-\infty}^{\infty}\left[(-i)^{\vartheta}J_{\vartheta}(kn_{cl}r)e^{i\vartheta\varphi}\right]\hat{z}. \tag{35}$$

To find the expressions for the internal fields in the TM polarization, $\vec{E}_{I\_TM}$ and $\vec{H}_{I\_TM}$, the generating function inside the cylinder is the same as the one for the incident field but with n_{co} as the refractive index for the core. Therefore, for the TM polarization the internal fields are:

$$\vec{E}_{I\_TM} = E_0 \sum_{\vartheta=-\infty}^{\infty} \left[C_\vartheta (-i)^\vartheta e^{i\vartheta\varphi} J_\vartheta(kn_{co}r) \right] \hat{z}, \tag{36}$$

$$\vec{H}_{I\_TM} = \sqrt{\frac{\varepsilon_0}{\mu_0}} E_0 \sum_{\vartheta=-\infty}^{\infty} \left[C_\vartheta (-i)^{\vartheta+1} \left(\frac{i\vartheta n_{co}}{kr} J_\vartheta(kn_{co}r)\hat{r} - n_{co} J'_\vartheta(kn_{co}r)\hat{\varphi} \right) e^{i\vartheta\varphi} \right]. \tag{37}$$

Note that the internal fields include the incident fields too, as we mentioned before that the incident fields are everywhere, both inside and outside the cylinder.

For the scattered fields (for convenience) we consider the inverse direction of the fields comparing to the incident light with a minus sign. Since the scattered fields do not contain $r = 0$, Bessel function of the second kind is also a choice for the generating function [27]. Thus, a linear combination of them which are the Hankel functions of the first and second kind could also be a choice for expanding the fields. More precisely, according to the sign convention of the frequency for the outward electromagnetic wave, $e^{-i\omega t}$, Hankel function of the first kind that yields outgoing scattered waves is the proper choice for the generating function f [29]. Therefore, the scattered fields for the TM polarization can be written as:

$$\vec{E}_{S\_TM} = -E_0 \sum_{\vartheta=-\infty}^{\infty} \left[D_\vartheta (-i)^\vartheta e^{i\vartheta\varphi} H_\vartheta(kn_{cl}r) \right] \hat{z}, \tag{38}$$

$$\vec{H}_{S\_TM} = -\sqrt{\frac{\varepsilon_0}{\mu_0}} E_0 \sum_{\vartheta=-\infty}^{\infty} \left[D_\vartheta (-i)^{\vartheta+1} \left(\frac{i\vartheta n_{cl}}{kr} J_\vartheta(kn_{cl}r)\hat{r} - n_{cl} J'_\vartheta(kn_{cl}r)\hat{\varphi} \right) e^{i\vartheta\varphi} \right], \tag{39}$$

where $H_\vartheta(kn_{cl}r)$ is a Hankel function of the first kind of order ϑ. To derive the coefficient D_ϑ for the scattered fields we use the boundary conditions of Eq. (5) and Eq. (6) at $r = a$ in the sense that:

$$\begin{cases} \left(\vec{E}_{i\_TM}\right)_z + \left(\vec{E}_{S\_TM}\right)_z = \left(\vec{E}_{I\_TM}\right)_z \\ \left(\vec{E}_{i\_TM}\right)_\varphi + \left(\vec{E}_{S\_TM}\right)_\varphi = \left(\vec{E}_{I\_TM}\right)_\varphi \end{cases}, \qquad \begin{cases} \left(\vec{H}_{i\_TM}\right)_z + \left(\vec{H}_{S\_TM}\right)_z = \left(\vec{H}_{I\_TM}\right)_z \\ \left(\vec{H}_{i\_TM}\right)_\varphi + \left(\vec{H}_{S\_TM}\right)_\varphi = \left(\vec{H}_{I\_TM}\right)_\varphi \end{cases}, \tag{40}$$

For the TM polarization we need only the first equation of the electric fields and the second one of the magnetic fields in Eq. (40). Thus,

$$J_\vartheta(kn_{cl}a) - D_\vartheta H_\vartheta(kn_{cl}a) = C_\vartheta J_\vartheta(kn_{co}a),$$

and

$$-n_{cl} J'_\vartheta(kn_{cl}a) + n_{cl} D_\vartheta H'_\vartheta(kn_{cl}a) = -n_{co} C_\vartheta J'_\vartheta(kn_{co}a),$$

give us two equations with two variables. We solve these easily for D_ϑ:

$$D_\vartheta = \frac{n_{cl} J'_\vartheta(kn_{cl}a) J_\vartheta(kn_{co}a) - n_{co} J_\vartheta(kn_{cl}a) J'_\vartheta(kn_{co}a)}{n_{cl} H'_\vartheta(kn_{cl}a) J_\vartheta(kn_{co}a) - n_{co} H_\vartheta(kn_{cl}a) J'_\vartheta(kn_{co}a)}. \tag{41}$$

The internal and the scattered fields for the TE polarization follow the same analogy of the TM polarization. Therefore,

$$\vec{E}_{I\_TE} = E_0 \sum_{\vartheta=-\infty}^{\infty} \left[V_\vartheta (-i)^{\vartheta+1} \left(\frac{i\vartheta}{n_{cl}kr} J_\vartheta(kn_{co}r)\hat{r} - J'_\vartheta(kn_{co}r)\hat{\varphi} \right) e^{i\vartheta\varphi} \right], \tag{42}$$

$$\vec{H}_{I\_TE} = -E_0 n_{co}\sqrt{\frac{\varepsilon_0}{\mu_0}}\sum_{\vartheta=-\infty}^{\infty}\left[V_\vartheta(-i)^\vartheta J_\vartheta(kn_{co}r)e^{i\vartheta\varphi}\right]\hat{z}, \tag{43}$$

are the internal fields and

$$\vec{E}_{S\_TE} = E_0\sum_{\vartheta=-\infty}^{\infty}\left[W_\vartheta(-i)^{\vartheta+1}\left(\frac{i\vartheta}{n_{cl}kr}H_\vartheta(kn_{cl}r)\hat{r} - H'_\vartheta(kn_{cl}r)\hat{\varphi}\right)e^{i\vartheta\varphi}\right] \tag{44}$$

$$\vec{H}_{S\_TE} = -E_0 n_{cl}\sqrt{\frac{\varepsilon_0}{\mu_0}}\sum_{\vartheta=-\infty}^{\infty}\left[W_\vartheta(-i)^\vartheta H_\vartheta(kn_{cl}r)e^{i\vartheta\varphi}\right]\hat{z}, \tag{45}$$

are the scattered fields of the TE polarization. To find W_ϑ, we use the second equation of the electric fields and the first one of the magnetic fields in Eq. (40). Solving the two equations two variables system for W_ϑ gives:

$$W_\vartheta = \frac{n_{cl}J_\vartheta(kn_{cl}a)J'_\vartheta(kn_{co}a) - n_{co}J_\vartheta(kn_{co}a)J'_\vartheta(kn_{cl}a)}{n_{cl}H_\vartheta(kn_{cl}a)J'_\vartheta(kn_{co}a) - n_{co}H'_\vartheta(kn_{cl}a)J_\vartheta(kn_{co}a)}. \tag{46}$$

2.1.1. Cross sections

The electromagnetic energy flux of the electromagnetic waves can be given by the pointing vector $\vec{S} = \frac{1}{2}Re\{\vec{E}\times\vec{H}^*\}$ which is defined as a time-averaged flux of energy that crosses a unit area [9, 26]. Then, the rate of the electromagnetic energy crossing the boundary of a surface of area $2\pi RL$, which surrounds a volume of a depicted cylinder of radius *R*, in the radial direction is given by:

$$W = -RL\oint_0^{2\pi}\vec{S}\cdot\hat{r}\,d\varphi. \tag{47}$$

The poynting vector $\vec{S}$ at a location outside the cylindrical is given by:

$$\vec{S} = \frac{1}{2}Re\left\{\left(\overrightarrow{E_\iota} + \overrightarrow{E_S}\right)\times\left(\overrightarrow{H_\iota} + \overrightarrow{H_S}\right)^*\right\}. \tag{48}$$

Therefore, we define:

$$\begin{aligned}\vec{S}_i &= \frac{1}{2}Re\left\{\overrightarrow{E_\iota}\times\overrightarrow{H_\iota}^*\right\},\\ \vec{S}_s &= \frac{1}{2}Re\left\{\overrightarrow{E_s}\times\overrightarrow{H_S}^*\right\},\\ \vec{S}_e &= \frac{1}{2}Re\left\{\left(\overrightarrow{E_\iota}\times\overrightarrow{H_S}^*\right) + \left(\overrightarrow{E_S}\times\overrightarrow{H_\iota}^*\right)\right\},\end{aligned} \tag{49}$$

where $\vec{S}_e$ arises from the interaction between the scattered and the incident field which signifies the amount of energy that has been removed from the incident waves and $\vec{S}_s$ is the poynting vector of the scattered field. From that, the rate of energy that is absorbed by the cylindrical object in a nonabsorbing medium is given by $W_a = W_i - W_s + W_e$, where the components of the RHS can be obtained by substituting the corresponding poynting vector from Eq. (49) into Eq. (47), considering the fact that the rate should be always positive we can write:

$$\begin{aligned}W_i &= -RL\oint_0^{2\pi}\vec{S}_i\cdot\hat{r}\,d\varphi,\\ W_s &= RL\oint_0^{2\pi}\vec{S}_s\cdot\hat{r}\,d\varphi,\\ W_e &= -RL\oint_0^{2\pi}\vec{S}_e\cdot\hat{r}\,d\varphi.\end{aligned} \tag{50}$$

For a nonabsorbing medium, W_i is an integration of a conservative field ($\vec{S}_i$ is not dependent on the spatial variable) over a closed path, which is always zero. Thus:

$$W_a = W_e - W_s, \tag{51}$$

where sub-indices a and s denote the rate at which the energy is absorbed or scattered across the surface $A = 2\pi RL$. Dividing Eq. (51) by the intensity of the incoming light $I_i = \frac{1}{2}\sqrt{\frac{\varepsilon_0}{\mu_0}}{E_0}^2$, from the left of the equation, gives C_a, C_e and C_s the absorption, extinction and the scattering cross sections respectively in the way that $C_a = C_e - C_s$.

Dividing the cross sections by 2aL (the cross section of the depicted cylinder) gives the corresponding efficiencies Q_a, Q_e and Q_s. Thus, after deriving the cross products of Eq. (49) from the fields in Eqs. (31), (32), (38) and (39) for the TM polarization and Eqs. (34), (35), (44) and (45) for the TE polarization, and performing the integrations of Eq. (50), we find:

$$\begin{aligned} Q_{s\_TM} &= \frac{2}{ka}\sum_{\vartheta=-\infty}^{\infty}|D_\vartheta|^2, \\ Q_{e\_TM} &= \frac{2}{ka}Re\{\sum_{\vartheta=-\infty}^{\infty}D_\vartheta\}, \end{aligned} \tag{52}$$

where Q_{s_TM} and Q_{e_TM} are the scattering and the extinction efficiencies for the TM polarization and D_ϑ can be obtained by Eq. (41) and

$$\begin{aligned} Q_{s\_TE} &= \frac{2}{ka}\sum_{\vartheta=-\infty}^{\infty}|W_\vartheta|^2, \\ Q_{e\_TE} &= \frac{2}{ka}Re\{\sum_{\vartheta=-\infty}^{\infty}W_\vartheta\}, \end{aligned} \tag{53}$$

are the scattering and the extinction efficiencies for the TE polarization and W_ϑ can be substituted by Eq. (46). Then, for the absorption efficiency we can use the following relation from Eq. (51) for each polarization:

$$Q_a = Q_e - Q_s. \tag{54}$$

In the end, it is worth mentioning that it is time saving to use $D_\vartheta = D_{-\vartheta}$ and $W_\vartheta = W_{-\vartheta}$ to reduce the calculations in Eq. (52) and Eq. (53).

2.2. The Scattering Matrix Method (SMM)

The Scattering Matrix Method (SMM) is an implementation of the Fourier Modal Method (FMM), which solves the Maxwell's equations [30, 31], thus taking diffraction and interference of monochromatic light fully into account. In our modeling, light is a plane wave, and the period of the structure and angle of the incident light is defined in the simulation, as well as the wavelength of the incident light.

In this method, first the whole geometry is divided into a number of subdivisions which are invariant in one specific direction, here denoted as the *z* direction, in the sense that the refractive index of the material $n_j(x, y)$in each of the subdivision does not change in the *z* direction, which is singled out as the propagation direction of the incident light. These subdivisions are called *slices*. Next, the electric and the magnetic field are expanded in the modal form of:

$$\vec{E}_{xy}^{\,j}(\vec{x}) = \sum_{\vartheta} \vec{E}_{\vartheta}^{\,j}(x,y)\left(C_{\vartheta}^{j,+} e^{i\beta_{\vartheta}^{j} z} + C_{\vartheta}^{j,-} e^{-i\beta_{\vartheta}^{j} z}\right). \tag{55}$$

Here ϑ is the order of the mode and $\vec{E}_{xy}^{\,j}$ is the x and y components of the electric field in the slice j and $C_{\vartheta}^{j,+}$ and $C_{\vartheta}^{j,-}$ are the eigenmodes as the expansion coefficients. Such eigenmodes exist because of the invariance in the z-direction. For a system that is not invariant in the propagation direction of light (like a circular surface in 2D which is illuminated by light in its radial direction), SMM transforms the geometry into several small rectangles through a staircase approximation that totally represents the main geometry while each of the rectangles are invariant in the propagation direction (Fig. (6)). To achieve the convergence in the numerical modeling, large numbers of such slices are required. After this, we solve for the eigenmodes in Eq. (56) for each slice. This is done by projecting the Maxwell's equations into a matrix form, which yields an eigenfunction relation suitable for digital computers. For this projection, we use a Fourier basis in the numerical calculations.

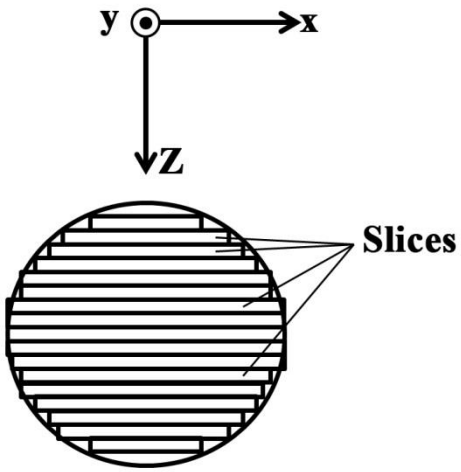

Figure 6. Schematic for a suitable transformation of a circle to many parallel rectangles for the scattering matrix method.

In the SMM, the incoming waves incident towards the system couple while the outgoing waves are scattered away from the system. Considering the boundary condition for the tangential part of the electric field at the interface of two neighboring slices, the next step in the SMM method is to couple eigenmodes in neighboring slices to each other, finally giving rise to coupling between the waves in the substrate and the superstrate:

$$\begin{bmatrix} C^{substrate,+} \\ C^{superstrate,-} \end{bmatrix} = S_{substrate\ to\ superstrate} \begin{bmatrix} C^{superstrate,+} \\ C^{substrate,-} \end{bmatrix}. \tag{56}$$

The operator $S_{substrate\ to\ superstrate}$ is called the scattering matrix; and $C^{superstrate,+}$ and $C^{substrate,-}$ are the expansion coefficients for the light incident light from the superstrate and the substrate toward the system while $C^{substrate,+}$ and $C^{superstrate,-}$ are outgoing waves out from the system from the substrate and the superstrate. This matrix contains all information about the geometry and physics/optics of the system. Assuming that the light is incident only from the superstrate and there is no incident light from the substrate, the starting points of the iteration can be fixed by $C^{substrate,-} = 0$ and $[C^{superstrate,+}]_j = \delta_{ij}$ where i denotes the index in the matrix for the incident plane wave, which is an eigenmode in the superstrate.

In this project, a large part of the effort was spent on solving the Maxwell's equations to obtain the absorption and the scattering cross sections of nanowires in an array. SMM is a very versatile method for such calculations since the absorption, reflection, and transmission properties can be readily obtained from Eq. (56)

In this project we use an implementation of SMM in MATLAB environment. The numerically optimized code was written previously by Nicklas Anttu, and modified in the present project for the case of an array of horizontal nanowires.

2.3. The Finite Element Method (FEM)

The Finite Element Method (FEM) is a numerical method for solving partial differential equations (PDEs) [32]. FEM approximates the PDEs with a discretized form of the original equation using a finite number of unknown parameters. In this way, FEM branches the *n*-dimensional domain of the geometry of problem comes from the dimension of the PDE to smaller *d*-dimensional subdivisions with $d \leq n$. Each such subdivision has a simple shape, for example, a line segment, a triangle or a tetrahedral in 1D, 2D and 3D domains (Fig. (7)), and these subdivisions are called mesh elements or finite elements. These elements do not overlap and meet each other at their boundaries. There are also nodes in the mesh elements which are points allocated at the vertices of the elements, and it is at these node points where the values of the dependent function are defined. From the knowledge of the dependent function at the node points, the values in the whole of the mesh element can be calculated through a predefined dependence on the locations (linear, quadratic, etc). Such additional node points may be to the system along the line segments for deriving a more precise solution at the cost of introducing additional unknown parameters.

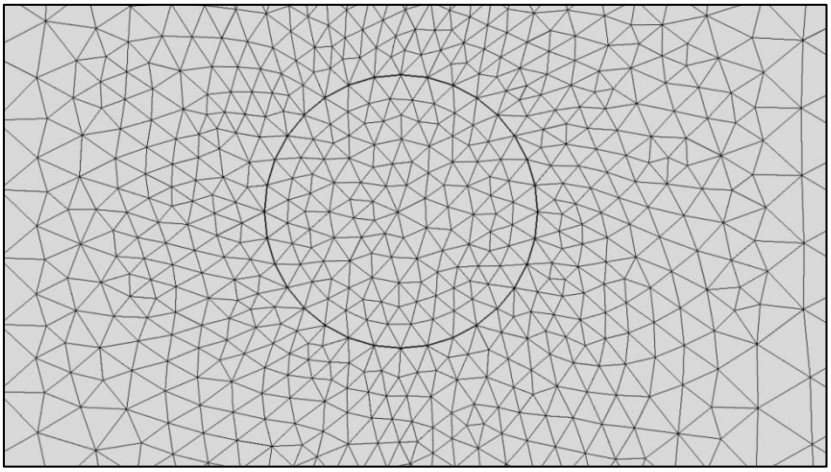

Figure 7. The mesh elements in The Finite Element Method for a circle in a free space.

In more detail, the FEM is a special case of the variational method. In electromagnetism, usually the PDE represents a relation for the fields, as is the case for example for the vector wave equation. Then the FEM obtains an energy related expression for the PDE, called a functional [33]. In general, a functional is an operation that attaches a value to each of a set of certain functions. If $u = f(s)$ is a set of functions on a continuous and differentiable surface like *S* that encloses the region *V*, then every other functions like *F* that assign a number for each *u* is a functional on the set *u* [32].

The trial solutions should be chosen then by the help of the potentials in the nodes which can be called the degrees of freedom. We should also choose a form for the interpolating functions that give the values for points outside the node points. The interpolating functions should be designed in such a way

that they satisfy the boundary values for the potentials at the nodes. After that, by minimizing the functional with respect to the potentials at the nodes, we make a system of equations in the number of degrees of freedom. By solving these equations, we obtain potential values at every point of the domain by the help of the pre-chosen interpolating function. After such calculation, one can convert the potential solution to the fields or other physical parameters of interest.

Since FEM finds the potential for each node in the domain directly, it is a fast and reliable method if one wants to study the fields. By the freedom in choosing adaptively the size and shapes of the mesh elements, it is also a very good method for systems with complex geometries. Another advantage of the FEM is that there are several commercially available software products that are designed to solve PDEs with a user friendly graphical interface using the FEM method. Thus, except for very specialized needs, there is no need of writing programming code, which could be very time consuming. One of the commercially available programs is COMSOL Multiphysics®, which solves varying types of physics problems with the FEM method. In this software, the user can design the desired geometry in a graphical interface and choose different mesh elements with a proper size and then attach a material to each geometry domain and apply the boundary conditions for the PDE as appropriate. There are also several advanced options for the solvers in COMSOL, for example to solve the problem directly or nonlinearly, or to handle the tolerance or define a maximum number for the iterations. In this work we use COMSOL Multiphysics® to solve the wave and the diffusion equations for complex geometries.

2.4. The Eigenfunction Method for Optical Waveguides

In this method, we try to find the propagating eigenfields and eigenmodes of a waveguide [28, 29, 34]. The total fields, can then be expanded by these propagating modes, which are the solutions to Maxwell's source free equations as:

$$\vec{E}(x,y,z) = \sum_{\vartheta} a_{\vartheta}\vec{E}_{\vartheta}(x,y,z) + \sum_{\vartheta} a_{-\vartheta}\vec{E}_{-\vartheta}(x,y,z) + \vec{E}_{rad}(x,y,z), \quad (57)$$

$$\vec{H}(x,y,z) = \sum_{\vartheta} b_{\vartheta}\vec{H}_{\vartheta}(x,y,z) + \sum_{\vartheta} b_{-\vartheta}\vec{H}_{-\vartheta}(x,y,z) + \vec{H}_{rad}(x,y,z), \quad (58)$$

where a_{ϑ}, $a_{-\vartheta}$, b_{ϑ} and $b_{-\vartheta}$ are the modal amplitudes, $\vec{E}_{\vartheta}$, $\vec{E}_{-\vartheta}$, $\vec{H}_{\vartheta}$ and $\vec{H}_{-\vartheta}$ are eigenfunctions and positive and negative signs of ϑ indicate forward and backward propagating modes in $+z$ or $-z$ direction, respectively (that is, along the axis of the cylinder) while index *rad* shows the radiation fields. Here, the radiation fields are the fields related to the spatial transient close to the source and before the spatial steady state along the fiber radiating out from the core to the cladding [28].

Defining β_{ϑ} as the eigenvalue or the propagation constant of the ϑth mode, and using the cylindrical symmetry of the system we can define the eigenmodes as:

$$\vec{E}_{\vartheta}(x,y,z) = \vec{e}_{\vartheta}(x,y)\exp(i\beta_{\vartheta}z), \quad (59)$$

$$\vec{H}_{\vartheta}(x,y,z) = \vec{h}_{\vartheta}(x,y)\exp(i\beta_{\vartheta}z). \quad (60)$$

Next step is to decompose the eigenmodes into transverse and longitudinal components corresponding to the waveguide axis. Considering only forward propagating modes, then the eigenmodes are:

$$\vec{E}_{\vartheta}(x,y,z) = (\vec{e}_{t\vartheta}(x,y) + e_{z\vartheta}(x,y)\hat{z})\exp(i\beta_{\vartheta}z), \quad (61)$$

$$\vec{H}_{\vartheta}(x,y,z) = (\vec{h}_{t\vartheta}(x,y) + h_{z\vartheta}(x,y)\hat{z})\exp(i\beta_{\vartheta}z), \quad (62)$$

where sub-indices *t* and *z* denote the fields in the transvers and longitudinal directions respectively. To the end of this chapter we only consider the modal fields. Therefore, we drop the modal index ϑ for simplicity.

To evaluate relations for longitudinal and transverse fields we should substitute Eq. (61) and Eq. (62) into the Maxwell equations (Eqs. (1)-(4)). But before, it is convenient to derive the following expressions for curls and divergences of the fields. From Eq. (57) we have:

$$\vec{\nabla}\times \vec{E} =\vec{\nabla}\times \left[(\vec{e}_t + e_z\hat{z})e^{i\beta z}\right] =\vec{\nabla}\times \left(\vec{e}_t e^{i\beta z}\right) +\vec{\nabla}\times \left(e_z e^{i\beta z}\hat{z}\right).$$

Using $\vec{\nabla}\cdot(\varphi\vec{a}) = \varphi\,\vec{\nabla}\cdot\vec{a} + \vec{a}\,\vec{\nabla}\,\varphi$, $\vec{\nabla}\times(\varphi\vec{a}) = \varphi\,\vec{\nabla}\times\vec{a} + \vec{\nabla}\,\varphi\times\vec{a}$ and $\vec{\nabla}\left(e^{i\beta z}\right) = i\beta e^{i\beta z}\hat{z}$ and $\vec{\nabla}n = 0$, we can write:

$$\vec{\nabla}\times \vec{E} = e^{i\beta z}\,\vec{\nabla}\times \vec{e}_t + e^{i\beta z}\left(-i\beta\vec{e}_t + \vec{\nabla}e_z\right)\times\hat{z}, \tag{63}$$

$$\vec{\nabla}\cdot \vec{E} = e^{i\beta z}(\vec{\nabla}\cdot\vec{e}_t + i\beta e_z). \tag{64}$$

Substituting Eq. (63) into Eq. (1) and Eq. (64) into Eq. (3) and separating longitudinal and tangential components yields:

$$\vec{h}_t(x,y) = \frac{1}{k}\sqrt{\frac{\varepsilon_0}{\mu_0}}\hat{z}\times\left(\beta\vec{e}_t(x,y) + i\vec{\nabla}e_z(x,y)\right), \tag{65}$$

$$\mathrm{h_z(x,y)} = \frac{-\mathrm{i}}{\mathrm{k}}\sqrt{\frac{\varepsilon_0}{\mu_0}}\hat{\mathrm{z}}\cdot(\vec{\nabla}\times\vec{\mathrm{e}}_\mathrm{t}(\mathrm{x},\mathrm{y})), \tag{66}$$

$$e_z(x,y) = \frac{i}{\beta}(\vec{\nabla}\cdot\vec{e}_t(x,y)). \tag{67}$$

The same expressions for curl divergence of the magnetic fields and substituting into Eq. (2) and Eq. (4) gives:

$$e_z(x,y) = \frac{i}{kn^2}\sqrt{\frac{\mu_0}{\varepsilon_0}}\hat{z}\cdot\left(\vec{\nabla}\times\vec{h}_t(x,y)\right), \tag{68}$$

$$\vec{e}_t(x,y) = -\frac{1}{kn^2}\sqrt{\frac{\mu_0}{\varepsilon_0}}\hat{z}\times\left(\beta\vec{h}_t(x,y) + i\vec{\nabla}h_z(x,y)\right), \tag{69}$$

$$h_z(x,y) = \frac{i}{\beta}\vec{\nabla}\cdot\vec{h}_t(x,y). \tag{70}$$

By substituting $\vec{h}_t$ [$\vec{e}_t$] from Eq. (65) [(69)] into Eq. (69) [(65)] we obtain very useful equations to derive the transverse components from the longitudinal components of the fields:

$$\vec{e}_t(x,y) = \frac{i}{(k^2n^2-\beta^2)}\left(\beta\vec{\nabla}e_z(x,y) - \sqrt{\frac{\mu_0}{\varepsilon_0}}k\hat{z}\times\vec{\nabla}h_z(x,y)\right) \tag{71}$$

$$\vec{h}_t(x,y) = \frac{i}{(k^2n^2-\beta^2)}\left(\beta\vec{\nabla}h_z(x,y) + \sqrt{\frac{\varepsilon_0}{\mu_0}}kn^2\hat{z}\times\vec{\nabla}e_z(x,y)\right) \tag{72}$$

To obtain the eigenfields for cylindrical waveguides we should solve the vector wave equation, $\nabla^2\vec{E} + k^2n^2\vec{E} = 0$ in the cylindrical coordinate where:

$$\nabla^2\vec{E} = \left(\nabla^2 e_r - \frac{2}{r^2}\frac{\partial e_\varphi}{\partial\varphi} - \frac{e_r}{r^2}\right)\hat{r} + \left(\nabla^2 e_\varphi - \frac{2}{r^2}\frac{\partial e_r}{\partial\varphi} - \frac{e_\varphi}{e_r}\right) + (\nabla^2 e_z)\hat{z}.$$

Now, using Eq. (71) and Eq. (72), we can derive transverse components $\vec{e}_r$ and $\vec{e}_\varphi$ from the longitudinal component $\vec{e}_z$. Thus, we only focus on solving the scalar wave vector equation $\nabla^2 e_z + k^2 n^2 e_z = 0$. Following the same procedure in solving Eq. (18) for *f* in Section 2.1 the general answer for e_z is:

$$e_z(r, \varphi, z) = L_\vartheta(knr)\emptyset(\varphi)\exp(\pm i\beta z). \tag{73}$$

Here $L_\vartheta(knr)$ is a Bessel function which we will modify it further and $\emptyset(\varphi) = \pm\sin(\vartheta\varphi)$ *or* $\emptyset(\varphi) = \pm\cos(\vartheta\varphi)$ with ϑ as an integer. β is the tangential component of the *K* vector of the incident field. From the boundary condition for plane waves (see Section 1.2) at the boundary of the waveguide the tangential component of the *K* vector, β, is same for both, the cladding and the core (Fig.(1b)). Also, β is the propagation constant or the eigenvalue of the guided modes in the waveguide. If γ_{cl} is the normal component of the *K* vector in the cladding, k_{cl}, then ${\beta}^2 + {\gamma_{cl}}^2 = {k_{cl}}^2$. If $\beta > k_{cl}$, γ_{cl} is imaginary and it gives an exponential decay in the radial direction in the cladding, therefore, the modes are bound to the core. On the other hand if $\beta < k_{cl}$, γ_{cl} is real, and we have oscillating radiative fields in the cladding, electromagnetic energy leaks out from the core via this radiation. In summary we have two different sets of modes depending on the value of β [28]:

$kn_{cl} < \beta \leq kn_{co}$, Bound modes,

$\beta < kn_{cl}$, Leaky modes.

Here, the incident light is normal to the axis and there is no propagation of light along the waveguide. Therefore, $\beta = 0$ and from the above conditions all the modes become leaky. To assign a right Bessel function to $L_\vartheta(knr)$ we come back to Eq. (22) which is the radial part of the scalar wave equation. Eq. (22) has two different answers depending on the sign of k^2n^2. For $n = n_{cl}$, outside the waveguide, $k^2n^2 > 0$ and considering the sign convention of the frequency for the outgoing waves (*-iωt*), the solution is the Hankel function of the first kind of order ϑ, $H_\vartheta(kn_{cl}r)$. Inside the core with $n = n_{co}$, considering the convergence of the solutions, the solution is the Bessel function of the first kind of order ϑ, $J_\vartheta(kn_{cl}r)$. Therefore:

$$e_z = A\emptyset_\vartheta(\varphi)\begin{cases}\dfrac{J_\vartheta(kn_{co}r)}{J_\vartheta(kn_{co}a)}, & 0 \leq r \leq a,\\[2ex] \dfrac{H_\vartheta(kn_{cl}r)}{H_\vartheta(kn_{cl}a)}, & r \geq a.\end{cases} \tag{74}$$

By the same analogy the *z* component of the magnetic field is:

$$h_z = B\emptyset_\vartheta(\varphi)\begin{cases}\dfrac{J_\vartheta(kn_{co}r)}{J_\vartheta(kn_{co}a)}, & 0 \leq r \leq a,\\[2ex] \dfrac{H_\vartheta(kn_{cl}r)}{H_\vartheta(kn_{cl}a)}, & r \geq a.\end{cases} \tag{75}$$

where *A* and *B* are complex constants and a is the radius of the core. The denominators in Eqs. (74) and (75) appear to maintain the continuity at the boundary of $r = a$. To obtain the transvers

components of the electric and magnetic fields we use Eqs. (71) and (72) respectively. With $\beta = 0$, Eq. (71) becomes:

$$\vec{e}_t(x,y) = \frac{-i}{(k^2 n^2)} \sqrt{\frac{\mu_0}{\varepsilon_0}}\, k\hat{z} \times \left(\hat{r}\frac{\partial}{\partial r} + \frac{1}{r}\frac{\partial}{\partial \varphi}\hat{\varphi}\right) h_z(x,y). \tag{76}$$

Knowing $\hat{z} \times \hat{r} = \hat{\varphi}$ and $\hat{z} \times \hat{\varphi} = -\hat{r}$ and substituting h_z from Eq. (75) into Eq. (71), gives the expressions for the tangential components of the electric fields:

$$e_r = B\emptyset'_{\vartheta}(\varphi)\frac{i}{kr}\sqrt{\frac{\mu_0}{\varepsilon_0}} \begin{cases} \frac{J_{\vartheta}(kn_{co}r)}{{n_{co}}^2 J_{\vartheta}(kn_{co}a)}, & 0 \le r \le a, \\ \frac{H_{\vartheta}(kn_{cl}r)}{{n_{cl}}^2 H_{\vartheta}(kn_{cl}a)}, & r > a, \end{cases} \tag{77}$$

$$e_{\varphi} = -B\emptyset_{\vartheta}(\varphi) i \sqrt{\frac{\mu_0}{\varepsilon_0}} \begin{cases} \frac{J'_{\vartheta}(kn_{co}r)}{n_{co}J_{\vartheta}(kn_{co}a)}, & 0 \le r \le a, \\ \frac{H'_{\vartheta}(kn_{cl}r)}{n_{cl}H_{\vartheta}(kn_{cl}a)}, & r > a. \end{cases} \tag{78}$$

For the transverse components of the magnetic field, using Eq. (72) with $\beta = 0$ gives:

$$\vec{h}_t(x,y) = \frac{i}{k}\sqrt{\frac{\varepsilon_0}{\mu_0}}\, \hat{z} \times \left(\hat{r}\frac{\partial}{\partial r} + \frac{1}{r}\frac{\partial}{\partial \varphi}\hat{\varphi}\right) e_z(x,y). \tag{79}$$

By substituting $e_z(x,y)$ from Eq. (74) into Eq. (79) we can write the expressions for h_r and h_{φ}:

$$h_r = -A\emptyset'_{\vartheta}(\varphi)\frac{i}{kr}\sqrt{\frac{\varepsilon_0}{\mu_0}} \begin{cases} \frac{J_{\vartheta}(kn_{co}r)}{{n_{co}}^2 J_{\vartheta}(kn_{co}a)}, & 0 \ll r \ll a, \\ \frac{H_{\vartheta}(kn_{cl}r)}{{n_{cl}}^2 H_{\vartheta}(kn_{cl}a)}, & r > a. \end{cases} \tag{80}$$

$$h_{\varphi} = A\emptyset_{\vartheta}(\varphi) i \sqrt{\frac{\varepsilon_0}{\mu_0}} \begin{cases} \frac{n_{co}J'_{\vartheta}(kn_{co}r)}{J_{\vartheta}(kn_{c0}a)}, & 0 \ll r \ll a, \\ \frac{n_{cl}H'_{\vartheta}(kn_{cl}r)}{H_{\vartheta}(kn_{cl}a)}, & r > a. \end{cases} \tag{81}$$

Noting that the prime sign represents differentiation with respect to the related argument, $kn_{cl}r$ or $kn_{co}r$.

The case of $\beta = 0$, decouples the magnetic and the electric field components. Careful look at Eq. (76) shows that $\vec{e}_t(x,y)$ only depends on $h_z(x,y)$ and not $e_z(x,y)$ anymore. The case is the same for Eq. (79) where $\vec{h}_t(x,y)$ only rests on $e_z(x,y)$. This decoupling frees us to choose *A* and *B* independently. By setting $A = 1$ and $B = 0$ we have $e_z = h_r = h_{\varphi} = 0$, which means that only transvers components of the electric field are nonzero and the magnetic field is parallel to the axis of the waveguide. This refers to the TE modes (Fig. (5)). On the other hand, setting $A = 0$ and $B = 1$ yields the TM modes which have $h_z = e_r = e_{\varphi} = 0$ in their fields components (see Section 2.1 for more details). It is worth pointing out that because both $\emptyset(\varphi) = \cos(\vartheta\varphi)$ and $\emptyset(\varphi) = \sin(\vartheta\varphi)$ are acceptable in Eqs. (77), (78), (80) and (81), there is a twofold degeneracy for each of the nonzero fields.

Each one of the boundary conditions from Eq. (5) and Eq. (6) which are the continuity of e_φ, e_z, h_φ and h_z at $r = a$, forms a φ independent eigenvalue equation which are all equivalent. Here we choose e_φ from Eq. (78) for TE modes and h_φ from Eq. (81) for TM modes, therefore eigenvalues for TE modes can be obtain from:

$$\frac{J'_\vartheta(kn_{co}a)}{n_{co}J_\vartheta(kn_{co}a)} = \frac{H'_\vartheta(kn_{cl}a)}{n_{cl}H_\vartheta(kn_{cl}a)}, \tag{82}$$

and for TM modes:

$$\frac{n_{co}J'_\vartheta(kn_{co}r)}{J_\vartheta(kn_{co}a)} = \frac{n_{cl}H'_\vartheta(kn_{cl}a)}{H_\vartheta(kn_{cl}a)}, \tag{83}$$

which we solve for *k*. However because the Hankel functions are complex and the Bessel functions are real, *k* becomes complex-valued, and we can assign its real part to the wave vector in the radial direction of the leaky mode resonance and its imaginary part to the electromagnetic energy radiation of the leaky mode. These modes are indicated by $TE_{\vartheta l}$ and $TM_{\vartheta l}$ with an azimuthal mode number, ϑ, which is the effective number of wavelengths around the circumference of the waveguide and a radial order number, *l*, as the number of radial field maxima in the waveguide in the way that for a certain ϑ, the first or the smallest root of Eqs. (82) and 83 is $l = 1$ and the second one is $l = 2$ and so on [17].

In general, in the Eigen-function method we solve the vector wave equation for the allowed eigenmodes inside the waveguide and not for the total electric and magnetic fields. In contrast, in the Mie theory we find the complete solutions for the fields outside and inside the waveguide and not the eigenmodes.

3. Results

3.1. Single Nanowires

3.1.1. The Absorption and Scattering Efficiency

The absorption efficiency Q_{abs} of an infinitely long horizontal InP nanowire with a circular cross section, for different radii from $r = 10$ nm to $r = 120$ nm is illustrated in Fig. (8). The incident light is a plane wave normal to the axis of the nanowire (Fig.(5)) in two different polarizations TE and TM. Then, the absorption efficiency can be calculated by the Mie theory from Eqs. (52)-(54). Notice that we have neglected any quantization effects that could affect the refractive index of the nanowire material for the smallest radii considered. Instead, the bulk refractive index of intrinsic InP is used for the nanowire material for all radii. The surrounding medium is air. The bandgap of InP is $\lambda_{bg} = 925$ nm. For this reason we have chosen to consider the wavelength range up to $\lambda = 950$ nm for the incident light.

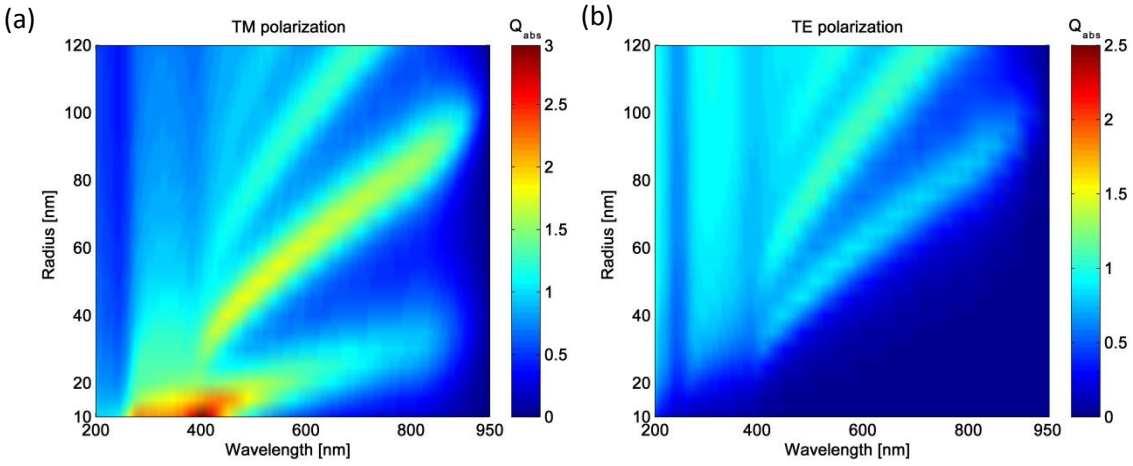

Figure 8. Absorption efficiency Q_{abs} of a single horizontal InP nanowire for (a) TE and (b) TM polarization of the incident light for the radius varying from 10 to 120 nm.

Due to the electrostatic limit the absorption of light by small nanowires is strongly polarization dependent, and that is clear from the Fig. (8). In more detail, for small nanowires in the TE polarization, the incident electric field is normal to the nanowire and experiences a large difference in the dielectric constants of the mediums at the interface and that leads to an attenuation in the electric field inside the nanowire according to $E_I = \frac{2\varepsilon_0}{\varepsilon+\varepsilon_0} E_i$, where ε is the dielectric constant of the nanowire, and E_I and E_i are the internal and external fields. On the other hand, for the TM polarization, the incident electric field is parallel to the axis of the nanowire and since the nanowire is assumed to be infinitely long, it does not suffer from the change in the dielectric constant of the mediums [35].

While the strength of the absorption efficiency in the TM polarization is different from the TE polarization, it has a different spectrum from TE polarization for radii smaller than 40 nm. Also Fig. (8) shows that the peaks of absorption undergo monotonous red shifts for larger radii and for wavelengths more than $\lambda = 400$ nm for both polarizations, which demonstrates the geometry dependence of absorptions in the nanowires. For wavelengths shorter than $\lambda = 400$ nm, we suspect that the absorption spectrum is not influenced much by the geometry and is dominated by the high values in the absorption coefficient γ of the bulk InP which is shown in Fig. (9a) and can be derived

from $\gamma = \frac{4\pi \cdot Im(n)}{\lambda}$, where $Im(n)$ is the imaginary part of the complex refractive index of the material and λ is the incident wavelength.

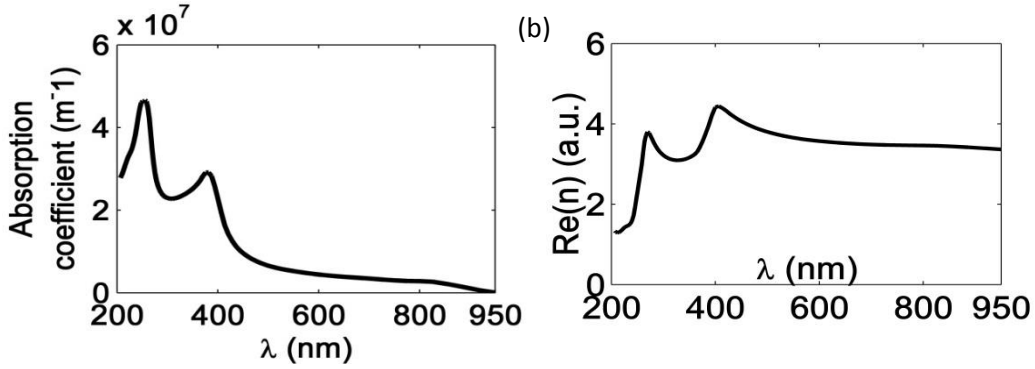

Figure 9. (a) Absorption coefficient and (b) real part of the refractive index of the intrinsic bulk InP [36].

For more detailed investigation in the absorption spectrum of Fig. (8), we assume that a nanowire can be seen as a single mode waveguide with a dielectric medium. Such a waveguide traps the normally incident light in its cross section much like a whispering gallery mode in a micro resonator [17, 37]. The trapped light has certain radiative eigenmodes that leak out the energy to the radiative far field that has been discussed thoroughly in Section 2.4. Considering the reciprocity between in- and out-coupling of light, incident light from the radiative far-field can couple strongly into these leaky modes which gives rise to the absorption spectrum in the position of the modes [38]. Thus we cut some lines from Fig. (7) in different radii and solve Eqs. (82) and (83) for each of them to find the $\mathrm{TM}_{\vartheta l}$ and $TE_{\vartheta l}$ modes. Then we compare the wavelength-positions of the eigenmodes with the wavelength position of the absorption peaks, as derived by the Mie theory when calculating the full absorption spectrum.

Fig. (10) shows the absorption efficiency for $r = 30$ nm and $r = 85$ nm. Here, for clarity we show for each radius and polarization not more than the three longest-wavelength modes. The wavelength position for these modes for wavelength shorter than $\lambda = 950$ nm are shown in Table.1.

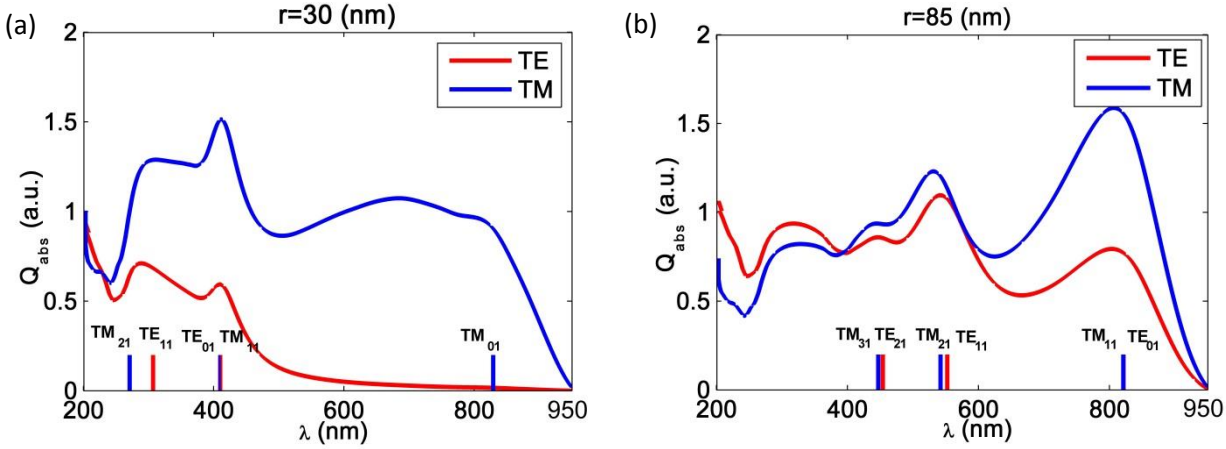

Figure 10. Absorption efficiency Q_{abs} for the TE and TM polarizations of nanowires with radii of (a) $\boldsymbol{r = 30}$ and (b) 85 nm

r (nm)	ϑl	TE modes (nm)	TM modes (nm)
30	01	410	829
	11	307	409
	21	131	271
85	01	821	-
	11	552	821
	21	454	542
	31	241	447

Table 1. The eigenmodes that show up at the longest wavelength for a circular InP nanowire with air as the surrounding medium for different radii $= 30$ and $r = 85$ nm.

It is clear from Fig. (10) and Tab. (1) that the modes undergo red shift as the radius of the nanowire increases from 30 nm to 85 nm. Also, the polarization dependence of absorption is stronger for shorter radius ($r = 30$ nm). On the other hand, absorption efficiency at $r = 85$ nm shows relatively the same peaks and dips in their spectra for both polarizations. Moreover, it is obvious that the shape of the absorption spectrum from Mie theory is dominated by the position of the eigenmodes. For example, for $r = 30$ nm, TM_{01} is placed at $\lambda = 829$ nm where a maximum appears in the absorption for the TM polarization, and it also happens for the other modes in both the nanowires. Furthermore, the red shift of the modes is apparent from the plots too. By increasing the radius of the nanowire, TM_{01} in $r = 30$ nm moves beyond the bandgap and therefore cannot couple with the incoming light in $r = 85$ nm, instead it is TM_{11} that takes its place at around $\lambda = 821$ nm. TE_{01} which was at $\lambda = 410$ nm for $r = 30$ nm, red shifts to $\lambda = 821$ nm where the TM_{11} is located.

Because Maxwell's equations are scaling invariant in the sense that scaling the geometrical dimensions by a factor of σ, scales the wavelength by the same factor so that λ transforms to $\sigma\lambda$, we expect a linear redshift of the wavelength-position of the eigenmodes while increasing the radius of the nanowire [17]. This redshift is illustrated in Fig. (11) for five different radii. We chose TE_{01}, because unlike the TM_{01} that crosses the bandgap quickly, TE_{01} has enough space in wavelength to travel before reaching the bandgap. Since the optical path should not change by changing the refractive index of the medium, the geometrical dimension is scaled by the real value of the refractive index *Re(n)* (see Section 1.1) that is shown in Fig. (9b) for the bulk InP. From Fig. (9b), we see relatively higher indices for wavelengths shorter than $\lambda = 500$ nm, where the optical path (geometrical dimension) decreases faster by higher values in its scaling factor *Re(n)*. This leads to a faster drop in the wavelength-position of the eigenmodes for shorter wavelengths which is apparent from Fig. (11).

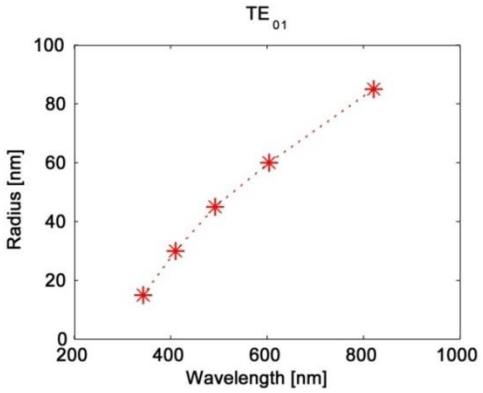

Figure 11. The positions of the TE_{01} mode of a circular InP nanowire for radius $r = 15$, 30, 45, 60 and 85 nm show a monotones redshift through the bandgap

The scattering efficiency is another important parameter for investigating the optical response of nanostructures. This can be done by calculating the Eqs. (52) and (53) from the Mie theory and is shown for $r = 30$ nm and $r = 85$ nm in Fig. (12). Comparing the results in Fig. (12) and Fig. (10) shows a relatively large scattering to absorption ratio for the wavelengths larger than $\lambda = 500$ nm which we will use it to justify some phenomena in the next chapters.

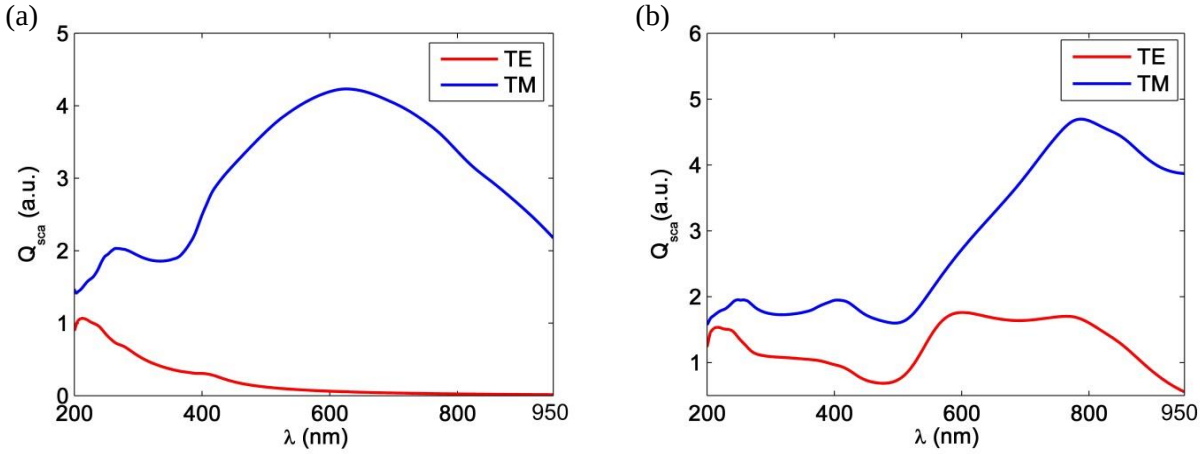

Figure 12. Scattering efficiency Q_{sca} for the TE and TM polarizations of nanowires with the radii of (a) $\boldsymbol{r = 30}$ and (b) 85 nm

3.1.2. Effects of the Refractive Index of the Surrounding Medium

To investigate the effects of the refractive index of the surrounding medium, we assume that the nanowire is inside a transparent nonabsorbing material such as Si_2O with a real constant refractive index of $n = 1.5$. In this case, since the system is still symmetric in the radial direction, the absorption efficiency can be calculated by the semi-analytical Mie theory from Eqs. (52)-(54). For the second case we assume that the nanowire is lying on the top of a thick layer of the same Si_2O. Thus, when one side of the medium is glass and the other side is air, the system is not symmetric in the azimuthal direction and its absorption efficiency cannot be calculated by Eqs. (52)-(54). Instead, for this case of a nanowire on a substrate, we solve the light scattering problem numerically with COMSOL Multiphysics. The results for $r = 85$ nm are shown in Fig. (13) for both polarizations together with the results from Fig. (10b) for the nanowire surrounded by air.

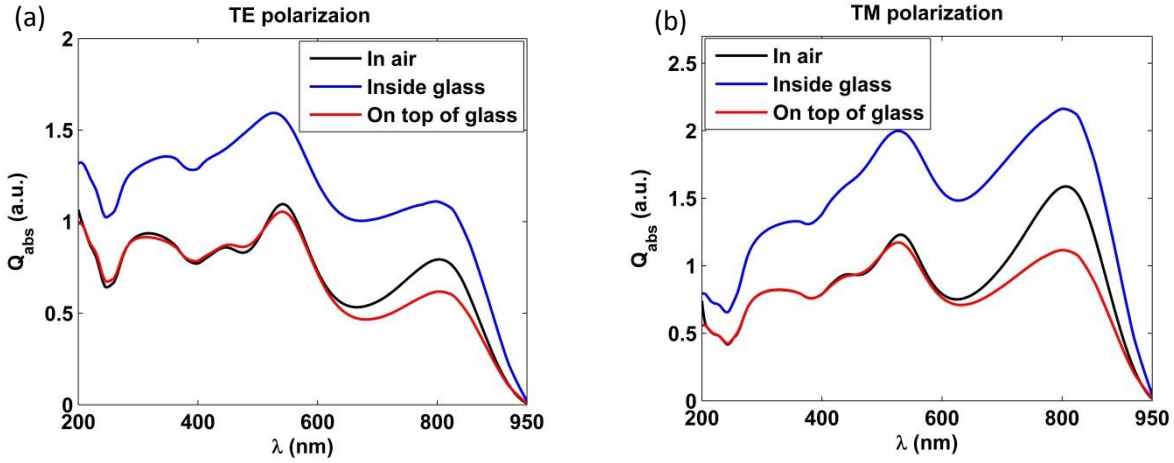

Figure 13. Absorption efficiency Q_{abs} for the (a) TE and (b) TM polarizations of a nanowire with the radius of $\boldsymbol{r = 85}$ nm in air, inside glass and on top of glass

From Fig. (13), we find that the wavelength-position of the modes in the nanowire do not vary much when the nanowire is placed on top of glass or inside glass, otherwise the peaks of the absorption would have shifted. However, the absorption is stronger if the glass covers whole of the nanowire comparing the case that the nanowire is on the top of glass or when the surrounding medium is air.

The reason that we consider the case of the nanowire on top of glass is for the applications of devices where the nanowires should be fixed on a substrate. We show in Fig. (13) that if the substrate is a nonabsorbing transparent material such as Si_2O, the absorption of light and the eigenmodes do not differ much from the case when the nanowire is surrounded by air. Therefore, the Mie theory for a symmetric system in the radial direction is a good assumption for such a design. In Appendix A we also discuss, through 3D electromagnetic modelling, how long a nanowire should be to yield a similar absorption spectrum as an infinitely long nanowire, in agreement with Mie theory. In other words, we show what the assumption of infinitely long nanowires means for applications. Another important issue that we investigate for the applications in the appendix B is a metallic contact that could be attached to the nanowire. We show that the absorption around the metal contact is highly influenced by the geometry of the metallic contact.

3.1.3. Eigenfields

To have more information about the origin of the peaks in the absorption efficiency, we study the eigenmodes in more detail, since it is the latter that give rise to the peaks. We plot Eqs. (74), (77) and (78) for the eigenmodes of Fig. (10a) for $r = 30$ nm in Fig. (14). As it is discussed thoroughly in Section 2.4, the phase dependency of the fields introduces a twofold degeneracy for the azimuthal order $\vartheta > 0$. Although any linear combination of these two polarizations is allowed, we show here the two independent forms of electric field for each eigenmode.

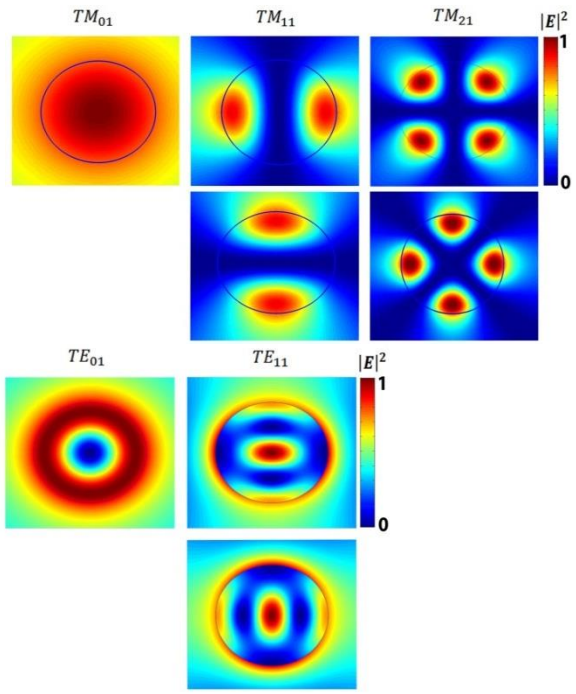

Figure 14. The electric field distribution $\left|\vec{E}\right|^2$ for TM_{01}, TM_{11}, TM_{21} and TE_{01} and TE_{11} for $r = 30$ nm. The eigenmodes are indicated in Fig.(3a). The values are normalized to $\left|\vec{E}\right|^2 = 1$

The eigenfields in Fig. (14), show how the electric field leaks out from the inside of the nanowire to its surrounding medium and also the fact that the very first eigenfields for both polarizations are relatively stronger than the others in the exterior of the nanowire.

3.2. The Periodic Array

The optical resonances in an infinitely long horizontal InP nanowire have been studied in the previous chapter. We saw how such resonances give rise to the shape of the absorption efficiency spectrum of the nanowire. In the following chapter we investigate the coupling of these optical resonances when a large number of nanowires are placed next to each other in a periodic array with a period of p as illustrated in Fig. (15).

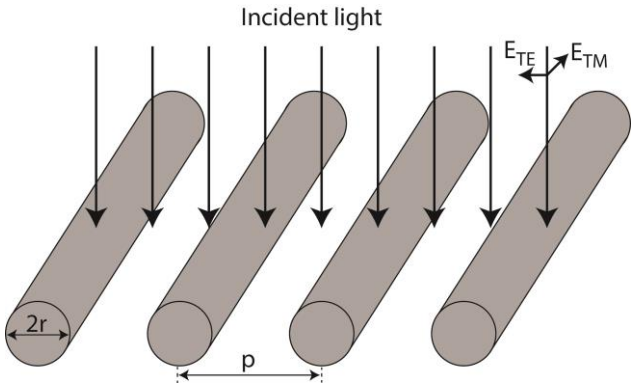

Figure 15. Schematic of an array of InP nanowires of radius r and period p. Notice that the normally incident TE (TM) polarized light has the electric field polarized perpendicular (parallel) to the axis of the nanowires.

3.2.1. Two Nanowires

First, we consider the case in which the array of Fig. (15) consists only of two nanowires and we calculate the absorption efficiency of one of them numerically with COMSOL Multiphysics (notice that in this symmetric configuration both nanowires show the same absorption efficiency). The results for the radius of $r = 85$ nm are shown in Fig. (16) for both TE and TM polarization. There, "*Distance*" shown on the *y* axis denotes the distance between the centers of the nanowires.

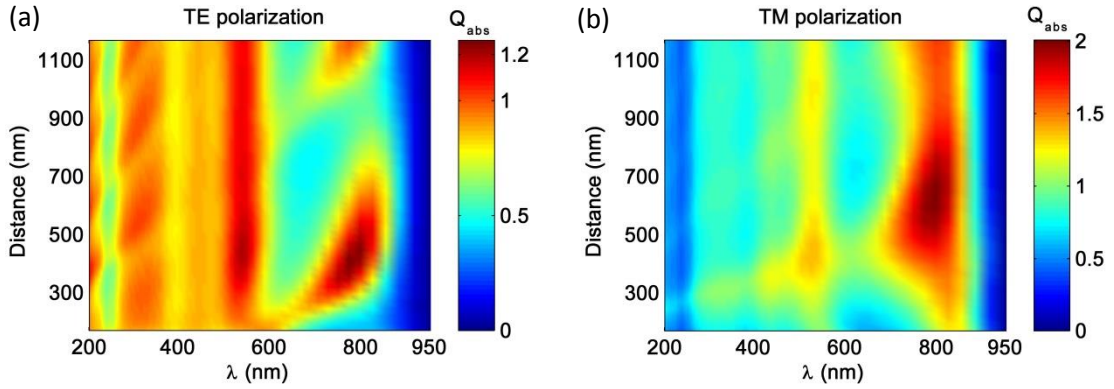

Figure 16. Absorption efficiency Q_{abs} of a nanowire in a horizontal InP bi-nanowire system with the radius of $r = 85$ nm for (a) TE and (b) TM polarization of the incident light. Here, air is the surrounding medium and "*Distance"* shown on the *y* axis denotes the distance between the centers of the nanowires. Notice the difference in the color bars between (a) and (b).

From Fig. (16), we see that for wavelengths approximately less than $\lambda = 500$ nm, except for a number of diagonal straight lines (discussed later), the absorption efficiency of either of the nanowires does

not vary much with the distance. Therefore, we can deduce that here the absorption efficiency of each of the nanowires is not influenced strongly by the scattering of light from the other nanowire. Instead, resonances arise from a single nanowire.

In strong contrast, the spectra show a clear dependency of the distance between the nanowires for wavelengths longer than $\lambda = 500$ nm. To study this distance dependence in more detail, we show three line-cuts for *Distance* = 170 nm, 395 nm and 695 nm in Fig. (17). We also show the absorption efficiency of a single, isolated nanowire (as calculated for Fig. (10b)). We see, as mentioned above in connection to Fig. (16), a shift in the modes for wavelengths approximately longer than $\lambda = 500$ nm for both polarizations. For the shorter wavelengths, the resonances are at the same positions as the modes for a single nanowire. We notice that the coupling and shift of optical resonances for the case when the two nanowires are placed close to each other (corresponding to Bi-170 nm in Fig. (17)) has been studied previously [38]. Here, we want to see how such coupling behavior of the modes shows up for a periodic structure.

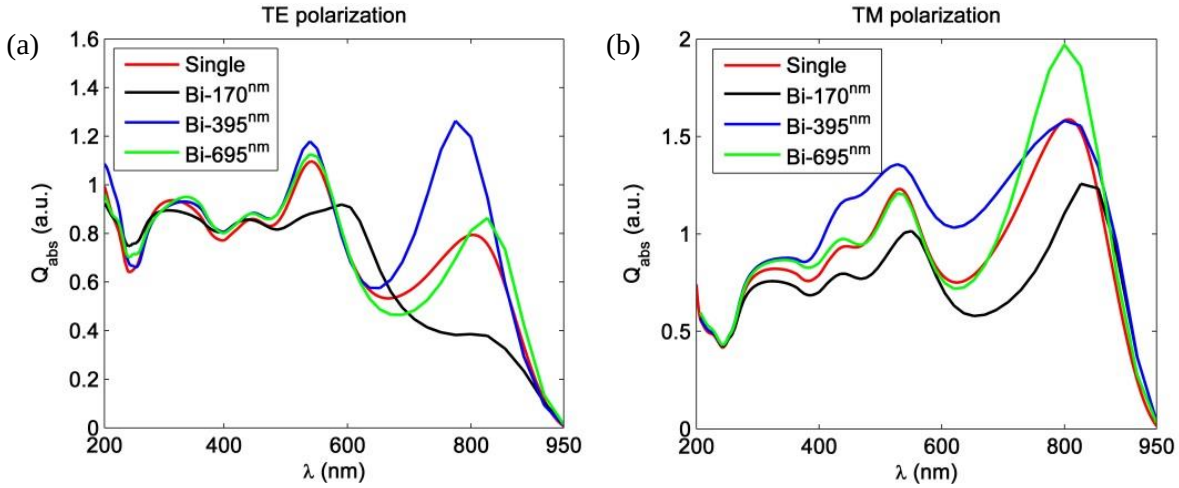

Figure 17. Absorption efficiency $\boldsymbol{Q_{abs}}$ of a horizontal InP bi-nanowire system with the radius of $\boldsymbol{r = 85}$ nm and air as the surrounding medium for (a) TE and (b) TM polarizations for different distances between their centers: 170 nm, 395 nm and 695 nm compared with the absorption efficiency of the single nanowire.

3.2.2. Periodic array

First, to find out how the response of the periodic nanowire array depends on the number of nanowires, we add nanowires one by one to the array and calculate the absorption of the one in the middle, numerically. In this way, we investigate how the convergence in the results is achieved and if it resembles the results from the simulation done with a periodic boundary condition, corresponding to an array of infinitely many nanowires. We found that a system with more than 20 nanowires, show an absorption spectrum that resembles very closely that of an array with infinitely many nanowires (denoted as *infinite periodic array* in the continuation). Some of these results for different number of nanowires (indicated as "*NWs"* in the figure) are shown in Fig. (18) for TE polarization with $r = 85$ nm. There, "*Period"* denotes the distance between the centers of two neighboring nanowires. From Fig. (18) one can notice that the straight lines, which appeared also in the two-nanowire system in Fig. (16a), have become more distinguishable in systems with more nanowires. We see here also how the peaks for the wavelengths longer than $\lambda = 500$ nm shift through the first line.

These diagonal straight lines that are due to the periodic structure of the array are the so-called lattice resonances. Such lattice resonances happen when the Bragg grating condition is fulfilled in the

nanowire array, which can be considered as an optical grating that scatters light. In this condition, a nanowire in the grating scatters constructively light to the neighboring nanowires, and resonances occur. In our case, the incident light is normal to the grating, and the resonances happen for wavelength-period combinations of $p = m\lambda$ with m an integer. Therefore, the shift of the peaks for long wavelengths, following the line $p = \lambda$, can be explained as the coupling of two different absorption resonances: single nanowire resonances and lattice resonances. This occurs when the wavelength of one of the lattice resonances, via tuning the period, coincides with the wavelength of one of the single nanowire resonances, which in turn can be tuned by changing the radius of the nanowire (as described in Section 3.1.1).

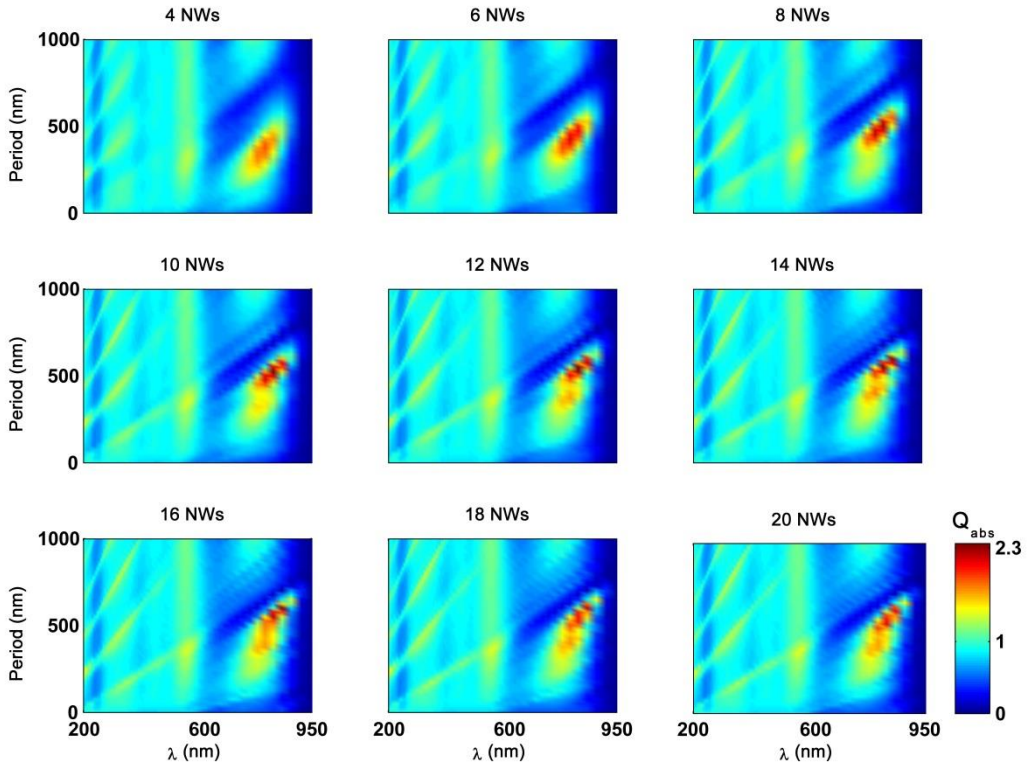

Figure 18. Absorption efficiency for an array of infinitely long horizontal InP nanowires with 4, 6, 8, …, 20 nanowires under normal illumination of TE polarized light. The absorption efficiency is calculated for the nanowires in the center of the array.

In Fig. (19) we see that this coupling of the two resonance types happens for both $r = 30$ nm and $r = 85$ nm and for both polarizations in an infinite periodic array. The spectra have been obtained by the SMM (Section 2.2). First we notice that in the vicinity of all the single-nanowire modes, the absorption spectrum shows a peak. Then we find that for $r = 30$ nm, there is a significant difference in the absorption of the two polarizations. In the TM polarization (Fig. (19c)), a strong coupling happens between the TM_{01} mode for a single nanowire and the lattice resonance, giving rise to the absorption efficiency of 6.1 at $\lambda = 906$ nm for $Period = 870$ nm, which is 18 times higher than the absorption efficiency of a single, isolated nanowire.

However, for the TE polarization (Fig. (19a)) we do not observe such a strong coupling through the TE_{01} mode, which is at $\lambda = 410$ nm for the single nanowire. We believe that the strong absorption coefficient of InP (Fig. (9a)) for $\lambda < 500$ nm leads complementarily to a weak scattering from each nanowire, which in turn yields a weaker coupling between the nanowires. Therefore, the spectrum in this short-wavelength region is dominated by the resonances of a single nanowire. In contrast, for

$\lambda > 500$ (where the TM_{01} mode shows up for r = 30 nm, Fig. (19c)), because of the relatively higher scattering to absorption cross-section (Fig. (19) and (12)), absorption and strong scattering can co-exist, leading to the coupling of the single nanowire resonances and the lattice resonances. Thus, to have a strong coupling which leads to strong absorption in the nanowires, we should tune the radius of the nanowires in such a way that one of the modes happens in $\lambda > 500$. This has been shown in Fig. (19) where, by increasing the radius from $r = 30$ nm to $r = 85$ nm in the TE polarization, the mode TE_{01} moves beyond the high absorptive area and can couple to the lattice resonance. This leads to an efficient absorption (Fig. (19b)) for a wavelength very close to the bandgap wavelength of InP, where the absorption in a single, isolated nanowire is almost negligible. On the other hand, from Figs. (19c) and (19d) for TM polarization, by increasing the radius of the nanowire to $r = 85$ nm, the TM_{01} mode red-shifts beyond the bandgap wavelength and vanishes. Instead, it is the TM_{11} mode that takes its place in the long wavelengths region and couples more freely with the lattice resonance, leading to a quite efficient absorption close to the bandgap relative to the single, isolated nanowire.

As seen clearly in Fig. (19), the absorption efficiency in the TM polarization for $r = 30$ nm in the vicinity of the longest-wavelength, TM_{01} mode (Fig. (19c)) is considerably stronger than in the vicinity of the other modes. We believe that the reason for this strong absorption lies in the electric field profile of the TM_{01} eigenmode as compared to that of the TE_{01} and TM_{11} modes in Fig. (19b) and (19d).

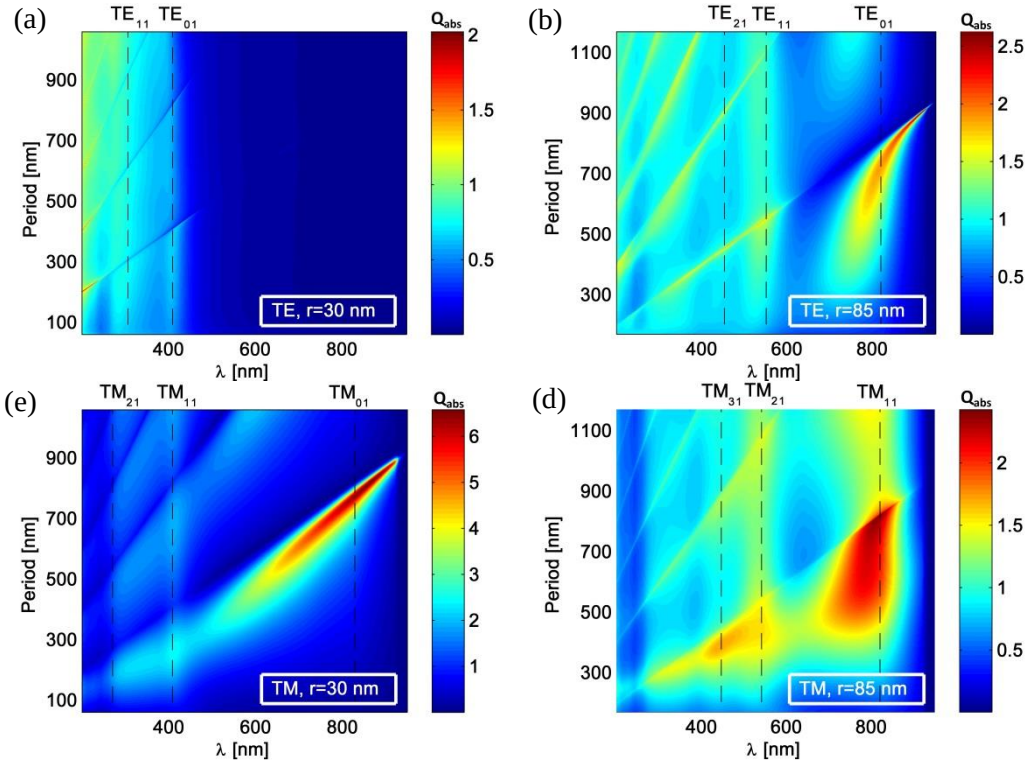

Figure 19. Absorption efficiency Q_{abs} for an infinite periodic array of infinitely long horizontal InP nanowires (Fig. (15)) for $r = 30$ nm with (a) TE and (c) TM polarizations and for $r = 85$ nm for (b) TE and (d) TM polarization. The modeling is performed by the SMM method (see Section 2.2 for more details).

Indeed, we find from Fig. (14) that the electric field outside the nanowire for TM_{01} mode is relatively stronger than the fields for the other modes. This means that the TM_{01} mode has the strongest scattering among the other modes, which leads to a stronger coupling with the lattice resonance.

Finally we want to compare the absorbance[1] A_{NW} (Eq. (87) of a nanowire in the infinite periodic array with the absorbance A_{TF} (Eq. (88) in a thin film that contains the same amount of InP material as the nanowire array:

$$A_{NW} = \frac{2r \cdot Q_{abs}}{P}, \tag{84}$$

$$A_{TF} = 1 - e^{-\gamma t(p)}, \tag{85}$$

where $\gamma = \frac{4\pi \cdot Im(n)}{\lambda}$ is the absorption coefficient of InP, $t(p) = \frac{\pi r^2}{p}$ is the thickness of the thin film and p is the period of the array (notice that we assume here that the thin film has a perfect anti-reflection coating both at the front and the back side). The results for this comparison are shown in Fig.(6) for two cases: (a) $r = 30$ nm with TM polarization and (b) $r = 85$ nm for TE polarization. Note that the results are shown here in the logarithmic scale, and we specifically show $log\left(\frac{A_{NW}}{A_{TF}}\right)$. First we find that the absorbance in the thin film is relatively stronger for short wavelengths. However, importantly, the nanowires absorb much stronger in the vicinity of the band gap wavelength where the thin film absorbs a very small amount of light. Here, in Fig. (20a) the nanowire absorbs 190 times more efficiently than the thin film at $\lambda = 922$ nm (the thin film absorbs only 0.18% of the incoming light) when the TM_{01} mode is located close to the band gap wavelength (λ_{bg} = 925 nm) for $r = 30$ nm. In Fig. (20b), instead, the TE_{01} mode is placed close to the band gap wavelength, and the nanowire absorbs 39 times more efficiently at $\lambda = 920$ nm than the same amount of InP in a thin film configuration where it absorbs only 1.78% of the incoming light.

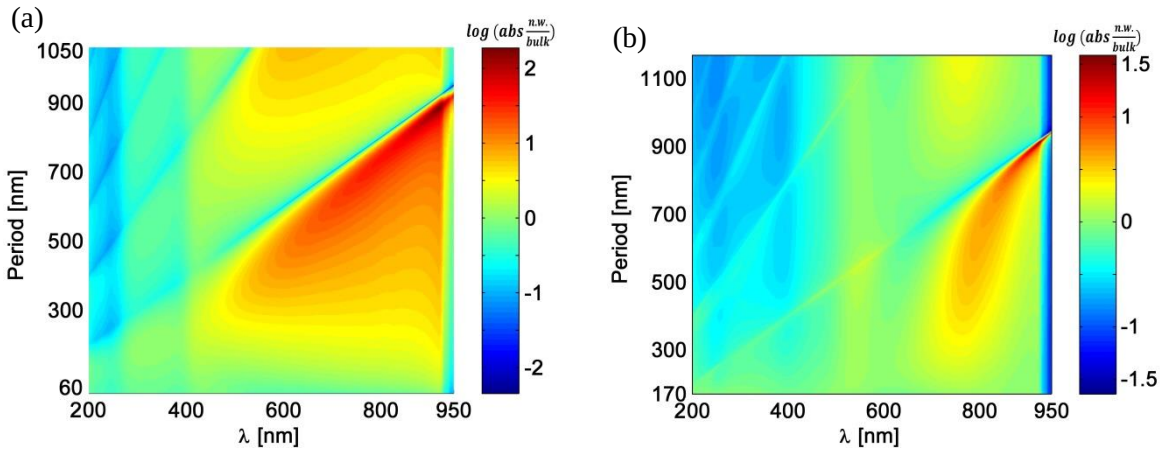

Figure 20. Absorbance A_{NW} for a periodic array of infinitely long horizontal InP nanowires relative to the absorbance A_{TF} in a thin film with the same amount of InP for (a) $r = 30$ nm with TM polarization and (b) $r = 85$ nm with TE polarization. The color bar is in logarithmic scale and shows $log\left(\frac{A_{NW}}{A_{TF}}\right)$.

3.2.3. Effects of the refractive index of the surrounding medium

The effect of the refractive index of the surrounding medium of a single nanowire on the light absorption has been studied in Section 3.1.2. Here, we summarize these effects for the periodic array of infinitely long horizontal InP nanowires for the specific case of $r = 85$ nm and TM polarization. The absorption efficiency in this case with air as the surrounding medium is shown in Fig. (18d). In Fig. (21), we show the results for the absorption efficiency of the same system with (a) SiO_2 (glass) as

[1] The absorbance $A(\lambda)$ is defined as the fraction of incident intensity of wavelength λ that is absorbed by the absorbing structures, which is here either the nanowire array or the thin-film.

the nonabsorbing transparent surrounding medium with real-valued and constant refractive index of $n = 1.5$ and (b) the array placed on top of a planar glass substrate.

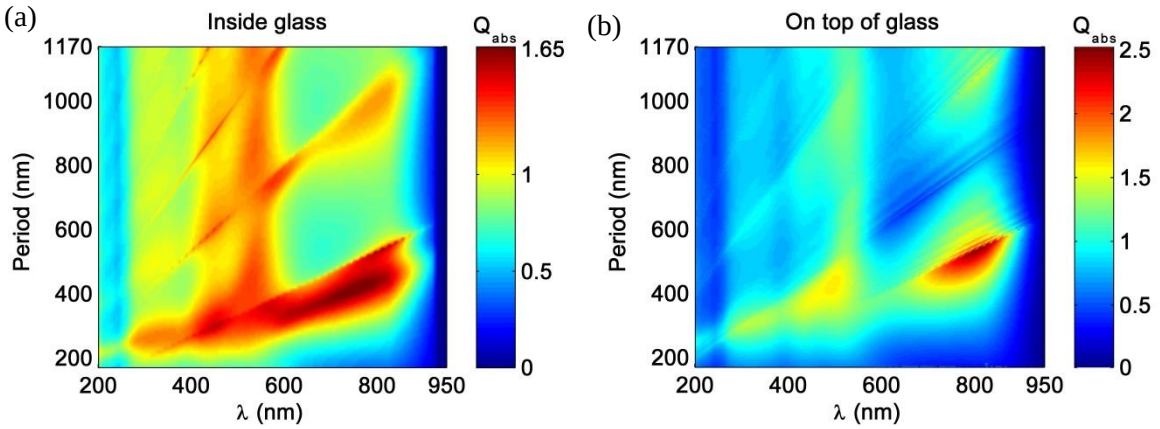

Figure 21. Absorption efficiency Q_{abs} for a periodic array of infinitely long horizontal InP nanowires with $r = 85$ nm for TM polarizaion with (a) SiO_2 as the surrounding medium with refractive index of $n = 1.5$ and (b) the array located top of a planar glass substrate.

By comparing the results shown in Fig. (21a) and Fig. (18c), we notice that the slope of the straight lines of the lattice resonances are 1.5 times steeper when the surrounding medium is air. This is due to the change in the Bragg grating condition to $p = m\frac{\lambda}{n}$ in case of glass surrounding the nanowires, with m an integer and $n = 1.5$, the refractive index of glass. Therefore, the coupling between the single nanowire modes and the lattice resonances happens for a smaller period for a given wavelength when glass surrounds the nanowires. Moreover, in the presence of glass, the nanowires in the array do not absorb long-wavelength light as efficient as nanowires surrounded by air. We believe that this weaker absorption could be due to the relatively higher absorption in the single nanowires inside glass compare to the ones in the air for long wavelengths (Fig. (13)). This high absorption could prevent the nanowires in the array surrounded by glass to scatter light as efficiencly as the nanowires surrounded by air and this leads to a weaker coupled resonance.

Finally, in Fig. (21b) we show results for the experimentally highly relevant system where the nanowire array is located on top of a planar glass substrate. We find that both lattice resonances, the ones for $n = 1$ (for the air on top of the nanowires) and those for $n = 1.5$ (for the glass substrate) show up in the spectrum. Here, the single nanowire modes couple partly with the lattice resonances in the glass substrate and partly with the lattice resonances in the air on top of the nanowires. We note however, the most efficient absorption happens approximately in the same wavelength as for an array in the air (Fig. (19d)), but with 1.5 times smaller period with almost the same value for Q_{abs}.

4. Conclusion and Outlook

In this project, we have investigated the interaction of light with nanostructures, with focus on the absorption in two different systems: an infinitely long horizontal InP single nanowire and a periodic array of such nanowires. This is done by solving the Maxwell equations and applying the boundary conditions of the incident light with different methods, suitable for each case. We believe that the results are of interest for the photodetection with nanowires, especially for wavelengths close to the band gap wavelength.

In this thesis, we first show how normally incident transverse electric and transverse magnetic polarized light excite the leaky modes TE_{0l} and TM_{0l}, respectively, in an isolated, single InP nanowire (Section 2.4 and 3.1). We also found that these resonances can be tuned by the radius of the nanowire. An increase in the radius, leads to redshifts in the eigenmodes monotonously (Section 3.1.1).

When moving to study the optical response of an array with infinitely many nanowires (infinite periodic array) we find that the periodic structure introduces new resonances to the optical response. These resonances are called lattice resonances, and take place by virtue of to the Bragg grating condition, which happens when light is scattered constructively from a nanowire to the neighboring nanowires. For normally incident light, we expect the resonances to arise for wavelength-period combinations of $p = m\lambda$ with m an integer, λ the wavelength of the incident light and p the period of the structure (Fig. (15)). Therefore, this kind of a resonance can be tuned by the period of the structure (Section 3.2.2).

Under specific circumstances, by tuning the radius of the nanowires and the period of the array, the single nanowire resonances can couple with the lattice resonances. This coupling can lead to a very efficient absorption of light by the nanowires (up to 18 times stronger than for the isolated single nanowires and 190 times stronger than for the same amount of material in a thin film discussed in Section 3.2.2). To engineer such resonant absorption, first, we consider the fact that the absorption coefficient of the bulk InP shows high values for wavelengths shorter than λ = 500 nm (Fig. (9a)). This leads to a strong non-resonant absorption in the single nanowires, which yields weaker scattering of light by the nanowires in the array. Such weak scattering leads in turn to a weaker optical coupling between the single nanowire modes and a weak excitation of the lattice resonance. Thus, we expect resonances for λ>500 nm and study the wavelength position of the single-nanowire modes at λ>500 nm.

Second, we use the fact that the TM_{01} mode scatters light stronger than the other TE_{0l} and TM_{0l} modes (Fig. (14)). Therefore, we observe, for λ > 500 nm, stronger coupling of the TM_{01} mode with the lattice resonance than for the other single-nanowire modes (Fig. (19)). This strong and efficient light absorption for long wavelengths can be of great interest in photodetection applications: Semiconductors show generally a relatively weak absorption coefficient close to their band gap wavelengths and for a conventional thin-film detector a large amount of semiconductor material is required to detect photons with high probability. Here, to detect TM polarized photons of a wavelength close to the band gap wavelength, we place, by tuning the nanowire radius, the TM_{01} at wavelengths slightly below the band gap wavelength. Then, we increase the period of the array to make the first lattice resonance to couple with the TM_{01} mode, so that the coupled resonance shifts toward the band gap wavelength. In case we wish to detect unpolarized light, it is instead suitable to use the TE_{01} and TM_{11} modes that show up close to each other (Tab. 1) and place them close to the band gap wavelength for corresponding coupling with the lattice resonances.

We also considered the refractive index of the surrounding medium as an additional parameter for enhancing the absorption of light. Two different cases have been studied in this work. One is when the nanowires are located inside SiO_2 (glass) and the other is when the nanowires are placed on top of a planar glass substrate. Although we see that the glass in either case does not change the positions of the modes in the single nanowires (Fig. (13)), it affects the lattice resonances by modifying the Bragg grating condition, $= m\frac{\lambda}{n}$, where *n* is the refractive index of the medium. Thus, the lattice resonances couple with the single nanowire modes at $n = 1.5$ times smaller periods for a given wavelength (Fig. (21)).

When the array is inside glass, although the wavelength positions of the single nanowire modes do not change from the case with air as the surrounding medium, the absorption is stronger in the single nanowires for long wavelengths in the presence of the glass (Fig. (13)). This strong absorption leads to a weak coupling between the nanowires and to a weaker excitation of the lattice resonances. Therefore, generally the absorption in the case with the array inside glass is less efficient than in the array in air (Fig. (21a)).

The second case, which is a more practical case for experiments, is when the array is placed on top of glass. Since the absorption in the single nanowires in this case is not as high as in the first case (Fig. (13)), the optical coupling of the single nanowire resonances and the lattice resonances in the array is stronger and this leads in the end to a more efficient absorption of light by the nanowires in the array comparing to the first case. Moreover, we note that the single nanowire modes couple partly with the lattice resonances in the glass substrate and partly with the lattice resonances in the air on top of the nanowires, but the most efficient absorption happens when the single nanowire mode couples through the lattice resonance of the glass (Fig. (21b)). Therefore, the wavelength of the most efficient absorption in the array on top of glass is determined by the single nanowire modes and the period is determined by the refractive index of the substrate.

Since the assumption of having an infinite periodic array of infinitely long horizontal nanowires is more ideal than practical, several investigations could be done to understand the optical response of more experimentally relevant finite systems. Furthermore, there exists a need for numerical calculations to investigate the absorption efficiency of nanowires in a slightly randomly misaligned array, in order to probe the effect of possible experimental imperfections. Moreover, although we show how long a nanowire should be to be considered as an infinitely long nanowire in Appendix A, further numerical calculations should be done to investigate the effect of a finite, short length of the nanowires for the optical response of the array. A structure with parallel aligned arrays could be considered to study the coupling of the neighboring edges. Also, changing the cross section of the nanowires from circular to hexagonal, as is often the case for epitaxially fabricated nanowires, could be another outlook of this thesis.

Finally, although experimental studies are beyond the scope of this thesis, fabrication and characterization of a nanowire photodetector utilizing the coupled optical resonances described in this thesis would be the last and ultimate outlook of this project.

Appendix A. The Effect of The Length of The Nanowires

To be able to use the Mie theory discussed in Section 2.1, a cylindrically symmetric system with an infinitely long nanowire is needed. Here we investigate how long a nanowire should be to give the same absorption cross section spectrum as an infinitely long nanowire. Here, we use as a model system InAs nanowires to study absorption in a large wavelength range (InAs has a band gap energy of 0.34 eV). We use the refractive index of bulk InAs with the band gap wavelength of $\lambda_g \approx 3600$ nm for the nanowires [19, 36]. The results have been obtained numerically with Comsol Multiphysics via electromagnetic 3D simulation by calculating the total absorption in the nanowire and translating this into an equivalent absorption cross-section. We show the absorption efficiency for nanowires with r = 30 nm with different lengths for TE (Fig. (22a)) and TM (Fig. (22b)) polarization. The light is incident at normal angle to the axis of the nanowire, and the surrounding medium is air. We show results for $200 < \lambda < 1800$ nm. For the TE polarization, the position of the absorption peaks or, equivalently, the position of the modes, does not change with increasing length to radius ratio. This could be due to the lack of strongly excited modes in a small radius nanowire for TE polarization (Section 3.1.1). On the other hand for TM polarization, the wavelength-position of the modes shows a clear red-shift when the nanowire length increases from $l = 300$ nm to $l = 1200$ nm. But from Fig. (22b) it can be observed that if the nanowire length is around 40 times its radius, the assumption of an infinitely long nanowire, as used in the Mie theory (black curve), is a good approximation.

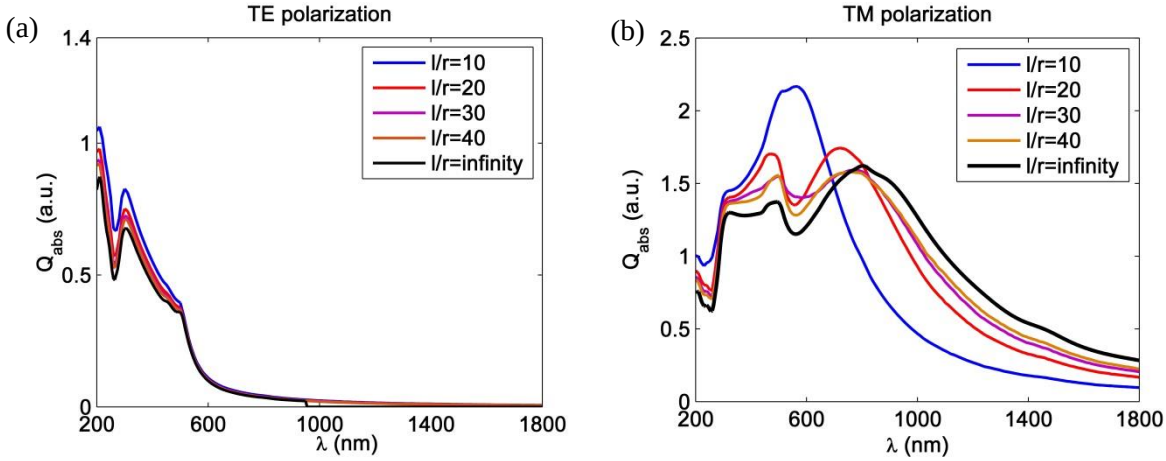

Figure 22. Absorption efficiency Q_{abs} for a single InAs nanowires under normal illumination for a radius of $r = 30$ nm and varying length of $l = 300$, 600, 900 and 1200 nm for (a) TE and (b) TM polarizations, together with the results for an infinitely long nanowire obtained by the Mie theory.

Next, we studied how the absorption varies along the axis of the nanowire in a finitely long nanowire. The results for $l = 500$ nm, 1000 nm and 2000 nm are shown together with the absorption efficiency in an infinitely long nanowire in Fig. (23) for the incident wavelength of $\lambda = 830$ nm (maximum absorption in Fig. (22b) for the infinitely long nanowire) for the TM polarization. Because of the symmetry of the nanowire, the origin of the plots has been placed in the middle of the nanowires, and we show results for only one half of a nanowire. One can mirror the spectrums horizontally to get the spectrum for the full length of the nanowires. From the results it appears that with increasing the length of the nanowire, the absorption spectrum gets closer to that for an infinitely long nanowire. Also, it can be observed that the absorption efficiency drops at the edges of the nanowire.

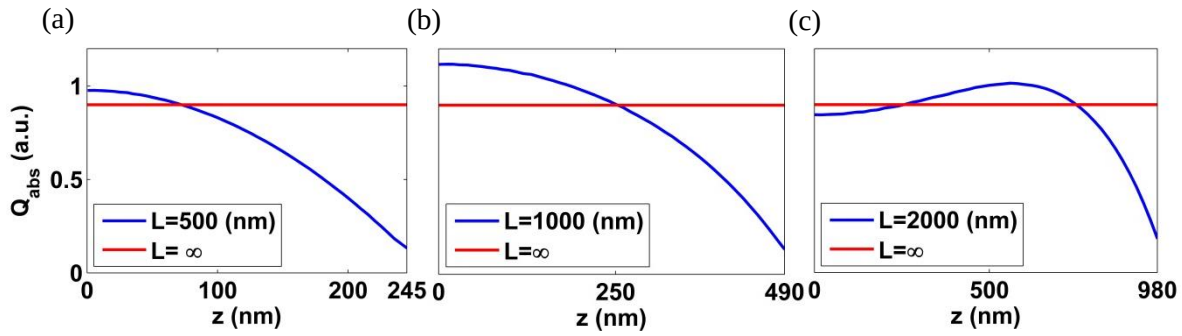

Figure 23. Absorption efficiency Q_{abs} for InAs single nanowires under normal illumination for a radius of $r = 30$ nm in the cross sections of the nanowires with lengths (a) $l = 500$ nm, (b) $l = 1000$ nm and (c) $l = 2000$ nm. The $z = 0$ corresponds to the middle of the nanowire. The incident light is TM polarized with $\lambda = 830$ nm and the surrounding medium is air.

Appendix B. The Effects of The Au Contact and Glass Substrate

In many applications, nanowires are contacted with a metal and placed on a substrate. Here, we investigate the effects of Au contact and glass substrate on the absorption efficiency of a 350 nm long InAs nanowire with the radius of $r = 30$ nm. The geometry of the system is shown in Fig. (24). The height of the contact is $H = 60$ nm in the tails and 50 nm above the contact. To decrease the load of the calculations, we have used the symmetry of the system and cut its width from the center and applied the appropriate boundary conditions for each polarization [39].

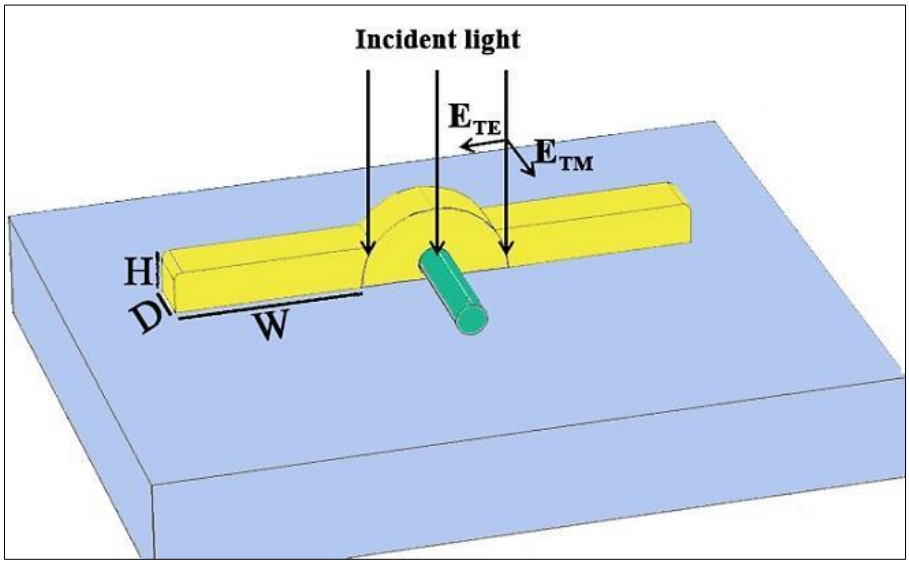

Figure 24. 350 nm long InAs nanowire with a radius of $r = 30$ nm (green cylinder) contacted with gold (indicated with yellow color) on glass substrate (blue area at the bottom). The height of the contact in the tail part is $H = 60$ nm, and the contact is 50 nm thick surrounding the nanowire. We have varied the width W and the depth D of the contact. A plane wave of light is incident normal to the axis of the nanowire. Different TE and TM polarizations of the light are also illustrated in the figure.

The normally incident light is chosen to be a plane wave (see Section 1.2 for more details). The absorption efficiency in the nanowire has been calculated by Comsol Multiphysics for both TE and TM polarization when the depth of the contact is D = 100 nm and when its width is W = 125 nm. The calculations were much heavier than the 2D simulations that have been done for the systems in chapter 3 (the time consumption for calculation of each wavelength-absorption point was almost 100 times more). The results are shown in Fig. (25). Comparing the absorption spectrums in Fig. (25) and Fig. (22) (the blue curve for $r = 300$ nm which is a 50 nm shorter nanowire), it can be seen that the absorption for the TE polarization does not vary much. However, for the TM polarization it shows a different spectrum. Although, the most efficient absorption occurs for the wavelengths between 300 nm and 700 nm, new optical resonances have been introduced to the spectrum, especially one at $\lambda \approx 1100$ nm. Considering that the glass substrate does not change the wavelength position of the modes for a single nanowire (see Section 3.1.2 for more details), we deduce that the effect of the Au contact for a short nanowire is more complicated than just simply providing a non-transparent cover to make the nanowire to appear shorter to the incident light.

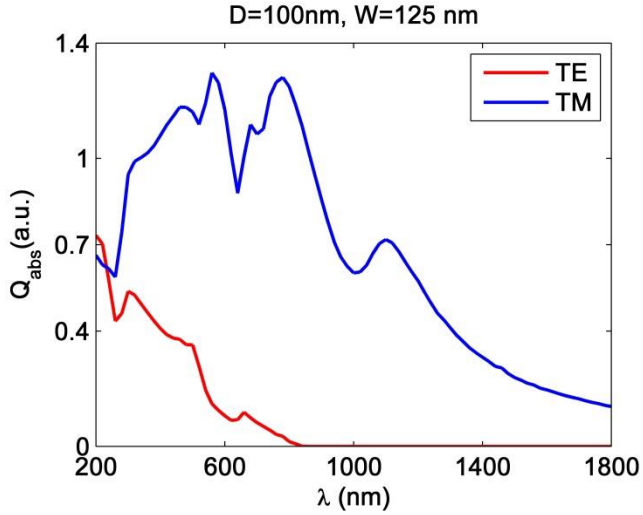

Figure 25. Absorption efficiency Q_{abs} for a single InAs nanowire (see Fig. (24) for a schematic) with the depth and the width of the contact $D = 100$ nm and $W = 125$ nm, respectively, for both TE and TM polarizations.

To study this effect in more detail, we changed the geometry of the contact. In Fig. (26a), we show result for a change in the depth of the contact to $D = 50$ nm and 100 nm keeping the width constant at $W = 360$ nm. In the results shown in Fig. (26b), we kept instead the depth constant at $D = 100$ nm and changed the width to $W = 0$ nm, 125 nm and 360 nm. The results are compared with the nanowire without contact (the gray curves). These results show a strong dependency of the resonances introduced by the contact, which we denote as *contact resonances*, on the geometry of the contact. We believe that these contact resonances are due to resonant oscillation of the electron gas in the metal, which are called surface plasmon resonances [40]. We also think that this geometry dependency of the resonances could be used as an additional parameter to tune and optimize the absorption in the nanowire devices.

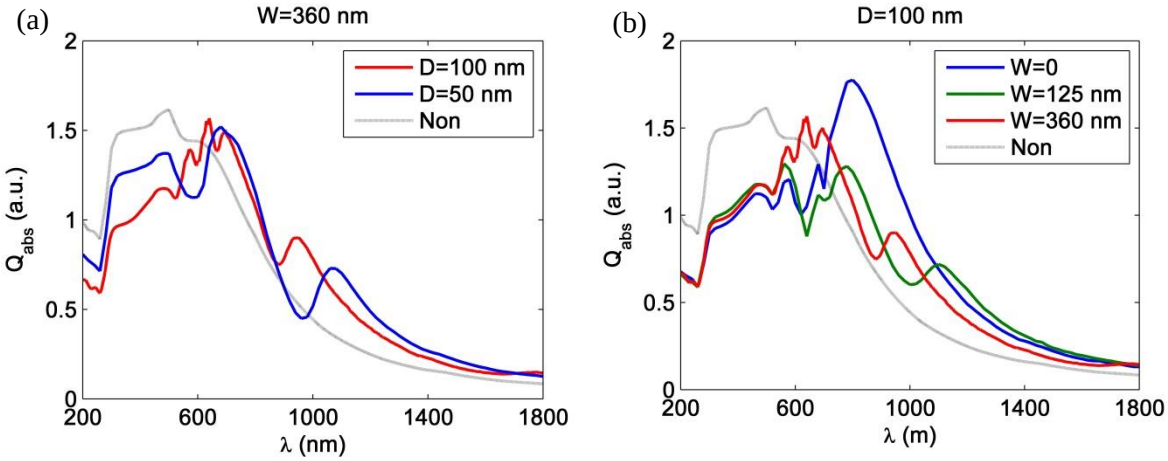

Figure 26. Absorption efficiency Q_{abs} for a single InAs nanowire (see Fig. (24) for a schematic) for (a) the contact with the width of $W = 360$ nm and depth of $D = 50$ nm (blue curve) and $D = 100$ nm (red curve) and (b) with the depth of $D = 100$ nm and width of zero (blue curve), $W = 125$ nm (green curve) and $W = 360$ nm (red curve). The incident light is TM polarized. In both (a) and (b) we show results also for a nanowire without any contact (gray curve).

To include the possible effect from the glass substrate into our analysis and to study the effect of the optical properties of the contact material, we compared the absorption efficiency for a nanowire surrounded by air and without a contact (red curve), the nanowire on the glass substrate without a contact (blue curves), the nanowire contacted with a material with same properties of Au but with very

high imaginary part of the refractive index $Im(n) = 50$ (green curve) and the nanowire with a normal gold contact (black curve) in Fig. (27a). The choice of the high absorbing contact ($Im(n) = 50$) has been made to see if we can suppress the resonances due to the surface plasmons, by dampening the excitation of the surface plasmon by increased losses due to absorption. The polarization is TM, and the light is normally incident. The length and the width of the contact are chosen to be $D = 100$ nm and $W = 360$ nm.

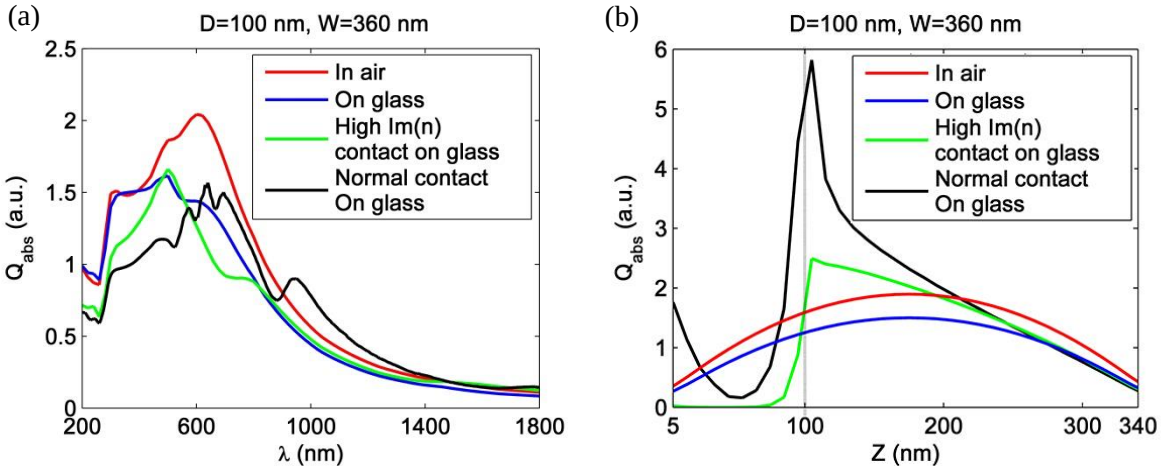

Figure 27. Comparing the absorption efficiency for a 350 nm long InAs nanowire (a) in air (red curve), on glass (blue curve), on glass with Au contact (Fig. (24)) with high imaginary part of the refractive index $Im(n) = 50$ (green curve) and with a normal Au contact (black curve) (a) for different wavelengths and (b) in the cross section along the axis of the nanowire for the wavelength $\lambda = 950\ nm$ where the origin is the edge of the nanowire which is under the contact. Therefore, the region to the left side of the gray line at $z = 100$ nm is the part of the nanowire that is under the contact.

From the results in Fig. (27a), it can be seen that the introduction of the glass substrate does not change the position of the modes and does not introduce new resonances, although it changes the absorption strength of the modes. Comparing the system with high absorbing contact (green curve) and the system with Au contact, it can be observed that the resonances in the latter are considerably suppressed in the former. Therefore, to dampen the resonances introduced by the surface plasmons of a metallic contact like Au, one can use metal that absorbs stronger.

In Fig. (27b), we show the absorption efficiency for the same system as in Fig. (27a) but along the nanowire in the cross section along the axis of the nanowire for the wavelength $\lambda = 950$ nm (at the peak in the black curve of Fig. (27a)). The origin of the z axis is placed at the edge of the nanowire which is under the contact. The depth of the contact is $D = 100$ nm. Therefore, the first 100 nm along the z axis is under the contact (the region to the left of the vertical gray line). We see clearly that the part of the nanowire covered by the Au contact absorbs light (black curve) and the most efficient absorption happens at $z = 105$ nm, in the vicinity of where the Au contact ends. In contrast, the green curve shows that the absorption under a strongly absorbing contact is almost zero. Moreover, comparing the uncontacted systems (the black and the red curves) reveals that the glass substrate does not change the absorption distribution along the nanowire, although it lowers it slightly.

Self-reflection

I feel fortunate for firstly getting the opportunity to be involved in a project studying an unexplored area in physics, and secondly for our results which were so inspiring and promising that we submitted them as an article in a highly reputable journal. This gave me the experience of developing a simple idea to an academic research group project. Also I have experienced how to interpret the results in a technical yet understandable and popular way to be able to publish them in a reputable scientific journal.

In physics, specifically, I have learnt about the light interaction with small particles, explicitly nanowires. I explored different theories and methods investigating the scattering of the electromagnetic waves with structures that have sizes comparable with the wavelength of the waves. The Rayleigh–Jeans theory, the Mie theory, the eigenfunction method were the semi analytical theories and methods that have been employed to conduct the project.

Furthermore, most important parts of the thesis have been done by numerical methods in electromagnetism. There, I have studied and compared different methods in simulation and computer modeling, mostly the scattering matrix method (SMM) and the finite element method (FMM) for solving the Maxwell's equations. However, these methods can be implemented in other physics problems and that gives me the capability to deal with possible new problems through my academic carrier in the field of computational physics.

Bibliography

1. Cajori, F., *A History of physics in its elementary branches: including the evolution of physical laboratories*. 1899: The Macmillan Company.
2. Wang, H.-Z., et al., *The actual nature of light (I) reveal the mystery about the actual nature of light from Newton, Einstein to the recent mistakes.* Journal of Quantum Information Science, 2011. **1**(02): p. 54.
3. Wallentin, J., et al., *InP nanowire array solar cells achieving 13.8% efficiency by exceeding the ray optics limit.* Science, 2013. **339**(6123): p. 1057-1060.
4. Garnett, E.C., et al., *Nanowire solar cells.* Annual Review of Materials Research, 2011. **41**: p. 269-295.
5. Hu, L. and G. Chen, *Analysis of optical absorption in silicon nanowire arrays for photovoltaic applications.* Nano Letters, 2007. **7**(11): p. 3249-3252.
6. Kupec, J., R.L. Stoop, and B. Witzigmann, *Light absorption and emission in nanowire array solar cells.* Optics Express, 2010. **18**(26): p. 27589-27605.
7. Saleh, B.E.A. and M.C. Teich, *Fundamentals of photonics*. 2007: Wiley.
8. Jackson, J.D., *Classical electrodynamics*. 1975: Wiley.
9. Bohren, C.F. and D.R. Huffman, *Absorption and Scattering of Light by Small Particles*. 2008: Wiley.
10. Kittel, C., *Introduction to solid state physics*. 2004: Wiley.
11. Davies, J.H., *The physics of low-dimensional semiconductors: an Introduction*. 1998: Cambridge University Press.
12. Chopra, K., P. Paulson, and V. Dutta, *Thin-film solar cells: an overview.* Progress in Photovoltaics: Research and Applications, 2004. **12**(2-3): p. 69-92.
13. Zhai, T., et al., *A comprehensive review of one-dimensional metal-oxide nanostructure photodetectors.* Sensors, 2009. **9**(8): p. 6504-6529.
14. Vj, L., et al., *A perspective on nanowire photodetectors: Current status, future challenges, and opportunities.* Selected Topics in Quantum Electronics, IEEE Journal of, 2011. **17**(4): p. 1002-1032.
15. Brongersma, M.L., Y. Cui, and S. Fan, *Light management for photovoltaics using high-index nanostructures.* Nature Materials, 2014. **13**(5): p. 451-460.
16. Kempa, T.J., et al., *Semiconductor nanowires: a platform for exploring limits and concepts for nano-enabled solar cells.* Energy & Environmental Science, 2013. **6**(3): p. 719-733.
17. Cao, L., et al., *Engineering light absorption in semiconductor nanowire devices.* Nature Materials, 2009. **8**(8): p. 643-647.
18. De Abajo, F.G., *Colloquium: Light scattering by particle and hole arrays.* Reviews of Modern Physics, 2007. **79**(4): p. 1267.
19. Vurgaftman, I., J. Meyer, and L. Ram-Mohan, *Band parameters for III–V compound semiconductors and their alloys.* Journal of Applied Physics, 2001. **89**(11): p. 5815-5875.
20. Wagner, R. and W. Ellis, *Vapor-liquid-solid mechanism of single crystal growth.* Applied Physics Letters, 1964. **4**(5): p. 89-90.
21. Su, B., Y. Wu, and L. Jiang, *The art of aligning one-dimensional (1D) nanostructures.* Chemical Society Reviews, 2012. **41**(23): p. 7832-7856.
22. Wang, M.C. and B.D. Gates, *Directed assembly of nanowires.* Materials Today, 2009. **12**(5): p. 34-43.
23. Long, Y.-Z., et al., *Recent advances in large-scale assembly of semiconducting inorganic nanowires and nanofibers for electronics, sensors and photovoltaics.* Chemical Society Reviews, 2012. **41**(12): p. 4560-4580.
24. Johansson, J. and K.A. Dick, *Recent advances in semiconductor nanowire heterostructures.* CrystEngComm, 2011. **13**(24): p. 7175-7184.
25. Fan, H.J., P. Werner, and M. Zacharias, *Semiconductor nanowires: from self-organization to patterned growth.* Small, 2006. **2**(6): p. 700-717.
26. Haverkate, L. and L. Feiner, *Optical properties of cylindrical nanowires.* 2006.

27. Riley, K.F., P. Hobson, and S.J. Bence, *Mathematical methods for physics and engineering: a comprehensive guide*. 2006: Cambridge University Press.
28. Snyder, A.W. and J.D. Love, *Optical waveguide theory*. 1995: Chapman & Hall.
29. Celozzi, S., G. Lovat, and R. Araneo, *Electromagnetic shielding*. 2008: Wiley Online Library.
30. Anttu, N. and H. Xu, *Scattering matrix method for optical excitation of surface plasmons in metal films with periodic arrays of subwavelength holes.* Physical Review B, 2011. **83**(16): p. 165431.
31. Tsopanidis, S., *Light interaction with nano-materials*, in *Department of Physics; Solid State Physics*. 2014, Lund university: Lund, Sweden.
32. Salon, S. and M. Chari, *Numerical methods in electromagnetism*. 1999: Academic Press.
33. Reddy, B.D., *Introductory functional analysis: with applications to boundary value problems and finite elements*. 1998: Springer.
34. Bures, J., *Guided optics*. 2009: John Wiley & Sons.
35. Wang, J., et al., *Highly polarized photoluminescence and photodetection from single indium phosphide nanowires.* Science, 2001. **293**(5534): p. 1455-1457.
36. Aspnes, D. and A. Studna, *Dielectric functions and optical parameters of Si, Ge, GaP, GaAs, GaSb, InP, InAs, and InSb from 1.5 to 6.0 ev.* Physical Review B, 1983. **27**(2): p. 985.
37. Cao, L., et al., *Resonant germanium nanoantenna photodetectors.* Nano Letters, 2010. **10**(4): p. 1229-1233.
38. Cao, L., P. Fan, and M.L. Brongersma, *Optical coupling of deep-subwavelength semiconductor nanowires.* Nano Letters, 2011. **11**(4): p. 1463-1468.
39. Kupec, J. and B. Witzigmann, *Computational electromagnetics for nanowire solar cells.* Journal of Computational Electronics, 2012. **11**(2): p. 153-165.
40. Barnes, W.L., A. Dereux, and T.W. Ebbesen, *Surface plasmon subwavelength optics.* Nature, 2003. **424**(6950): p. 824-830.